Multiscale Modeling and Optimization of Seashell Structure and Material

by

Mostafa Yourdkhani

June 2009

Department of Mechanical Engineering

McGill University, Montreal, QC, Canada, H3A 2K6

A thesis submitted to McGill University
in partial fulfillment of the requirements of the degree of
Master of Engineering

McGill

Abstract

The vast majority of mollusks grow a hard shell for protection. Typical seashells are composed of two distinct layers, with an outer layer made of calcite (a hard but brittle material) and an inner layer made of a tough and ductile material called nacre. Nacre is a biocomposite material that consists of more than 95% of tablet-shape aragonite, $CaCO_3$, and a soft organic material as matrix. Although the brittle ceramic aragonite composes a high volume fraction of nacre, its mechanical properties are found to be surprisingly higher than those of its constituents. It has been suggested that calcite and nacre, two materials with distinct structures and properties, are arranged in an optimal fashion to defeat attacks from predators. This research aims at exploring this hypothesis by capturing the design rules of a gastropod seashell using multiscale modeling and optimization techniques. At the microscale, a representative volume element of the microstructure of nacre was used to formulate an analytical solution for the elastic modulus of nacre, and a multiaxial failure criterion as a function of the microstructure. At the macroscale, a two-layer finite element model of the seashell was developed to include shell thickness, curvature and calcite/nacre thickness ratio as geometric parameters. The maximum load that the shell can carry at its apex was obtained. A multiscale optimization approach was also employed to evaluate whether the natural seashell is optimally designed. Finally, actual penetration experiments were performed on red abalone shells to validate the results.

Résumé

Une vaste majorité des mollusques développent une coquille dure pour leur protection. Une coquille typique est constitué de deux couches distinctes. La couche externe est faite de calcite (un matériau dur mais fragile), tandis que la couche interne est composée de nacre, un matériau plus résiliant et ductile. La nacre est un matériau biocomposite constitué de plus de 95% d'aragonite sous forme de tablette et d'un matériel organique souple qui forme la matrice. Bien que la céramique aragonite constitue une grande portion de la nacre, ses propriétés mécaniques sont étonnamment plus élevées de celles de ses constituants. La calcite et la nacre, deux matériaux avec des propriétés et des structures différentes, sont supposément étalonnées de façon optimale pour combattre les attaques de prédateurs. Cette étude cherche à déterminer les règles de construction d'une coquille de gastropode en utilisant la modélisation multi-échelle et des techniques d'optimisation. À l'échelle microscopique, un volume représentatif de la microstructure de la nacre a été utilisé pour formuler une solution analytique de son module d'élasticité et un critère de fracture multiaxial fonction des dimensions de la microstructure. À l'échelle macroscopique, un modèle d'éléments finis à deux couches de la coquille à été utilisé pour représenter la curvature et le ratio calcite/nacre en fonction des paramètres géométriques. La charge maximale que la coquille peut supporter à son apex a été déterminée. Une approche d'optimisation multi-échelle a aussi été employée pour évaluer la reconstruction optimale du coquillage naturel. Finalement, plusieurs tests ont été effectués sur une coquille d'abalone rouge pour valider les résultats.

Acknowledgement

I would like to express my sincere gratitude to my advisors, Professors Francois Barthelat and Damiano Pasini, for their extensive guidance, encouragement and support during this research. They were always willing to provide me with scientific insights, expertise, and assistance.

Special appreciation goes to Mr. John Danby who helped me in preparing the experiment setup. I am grateful to Mr. Li-Jen Chen for training me for image correlation system. I would also like to thank Mr. Victor Feret who trained me for MTS machine.

I thank my colleagues from the Biomimetics and the Multiscale Design Optimization Group, for their assistance and discussion in group meetings, and also for their amiable friendship. Sincere thanks to Mr. Reza Rabiei, Mr. Hossein Ghiasi and Mr. Sacheen Bekah for their guidance, scientific insights and advice. Among other things, Sacheen helped me in translating the abstract.

Last but not least, endless thanks to my lovely family for their continuous and incredible support, love and encouragement in every step of my life.

Table of Contents

List of Figures

List of Tables

List of Symbols

A_{Tablet}	Cross sectional area of the tablet
E_i	Young's modulus of interface
$E_{In-plane}$	In-plane Young's modulus of nacre
$E_{Out-of-plane}$	Out-of-plane Young's modulus of nacre
E_t	Young's modulus of tablet
G_i	Shear modulus of interface
$G_{In-plane}$	In-plane shear modulus of nacre
$G_{Out-of-plane}$	Out-of-plane shear modulus of nacre
J_c	Toughness
L_t	Length of tablet
l_o	Length of tablet overlap
l_o^*	Length of tablet overlap normalized by the length of tablet
$P_{Initial}$	Initial load assumed for solving the finite element model
P_{Load}	Amount of load transferred via contact load distribution
P_m	Average contact pressure
$P_{\max}$	Maximum supportable load of the shell
P_w	Worst point of simplex
P^*	New point of simplex
$\overline{P}$	Centriod of simplex
R	Radius of curvature of shell
R^*	Radius of curvature of shell normalized by contact radius
r_p	Contact load radius
$S_{Calcite}$	Ultimate strength of calcite
$S_{Nacre-transverse}$	Transverse strength of nacre

t	Shell thickness
t_i	Thickness of interface
t_j	Thickness of junction
t_t	Thickness of tablet
t^*	Shell thickness normalized by contact radius
t_i^*	Thickness of interface normalized by length of tablet
t_t^*	Thickness of tablet normalized by length of tablet
u	Displacement
V	Volume fraction of tablet
α_c	Ratio of thickness of calcite layer to shell thickness
β	Opening angle of shell
ε_{RVE}	Strain of RVE
γ_{ix}	Shear deformation of interface
λ	Failure ratio
λ_F	Failure ratio for the whole structure
σ_i	Axial stress of interface
σ_{jun}	Stress transferred in junction
σ_o	Summation of tablets stresses at any cross section of nacre
$\sigma_{Nacre-eq}$	Equivalent stress of nacre determined by failure criterion
σ_{pr}	Principal stress
σ_{RVE}	Stress of RVE
$\bar{\sigma}$	Average stress of tablet
σ_i^y	Yield stress of interface
υ	Poisson's ratio of nacre
$\tau_{axial\ stress}$	Shear stress induced on interface due to global axial stress
$\tau_{external}$	Shear stress induced on interface due to global shear stress

τ_i	Shear stress of interface
ψ	Operation factor in simplex optimization method

Chapter I Introduction

Biological structures have been optimally designed for their living conditions through million years of evolution. Being composed of commonly found components, biological materials and structures reveal a unique composite design with remarkable mechanical properties. Tooth enamel, bone and spider silk are a few examples of biological materials that show outstanding mechanical performances despite the fact that their basic constituents are relatively weak.

1.1 Biomimetics

Humans have always striven to improve the performance and efficiency of their tools and devices. As an excellent source of inspiration, nature has opened a way for them to inspire new ideas for fabricating novel materials and structures. As a result, humans have always mimicked the unique mechanisms and particular features from biology to develop new methods and processes for synthesizing mane-made devices and materials. The link between the applied sciences and biology is called biomimetics [1]. Biomimetics was first defined in Webster's dictionary in 1974 as '*the study of the formation, structure or function of biologically produced substances and materials (as enzymes or silk) and biological mechanisms and processes (as protein synthesis or photosynthesis) especially for the purpose of synthesizing similar products by artificial mechanisms which mimic natural ones*'. Biomimetics is the science that studies the technology transfer from nature to synthesized man-made materials and structures. The mechanisms that enhance the performance of biological structures and materials are duplicated in biomimetics to produce artificial ones by using ordinary materials [1, 2].

The first attempt to copy from nature was made by the Chinese people 3000 years ago to make artificial silk [3]. Humans have also carefully observed how birds fly with the ultimate goal of designing better flying machines.

In the past decades, researchers and engineers have started to resort more systematically to biology for the design of artificial structures and materials. The following describes a few examples of recent achievements in bio-inspired technology.

Superhydrophobicity of lotus leaf. The lotus leaf has a water-repellent surface that possesses hydrophobic and self-cleaning properties (Figure 1-1) [3].

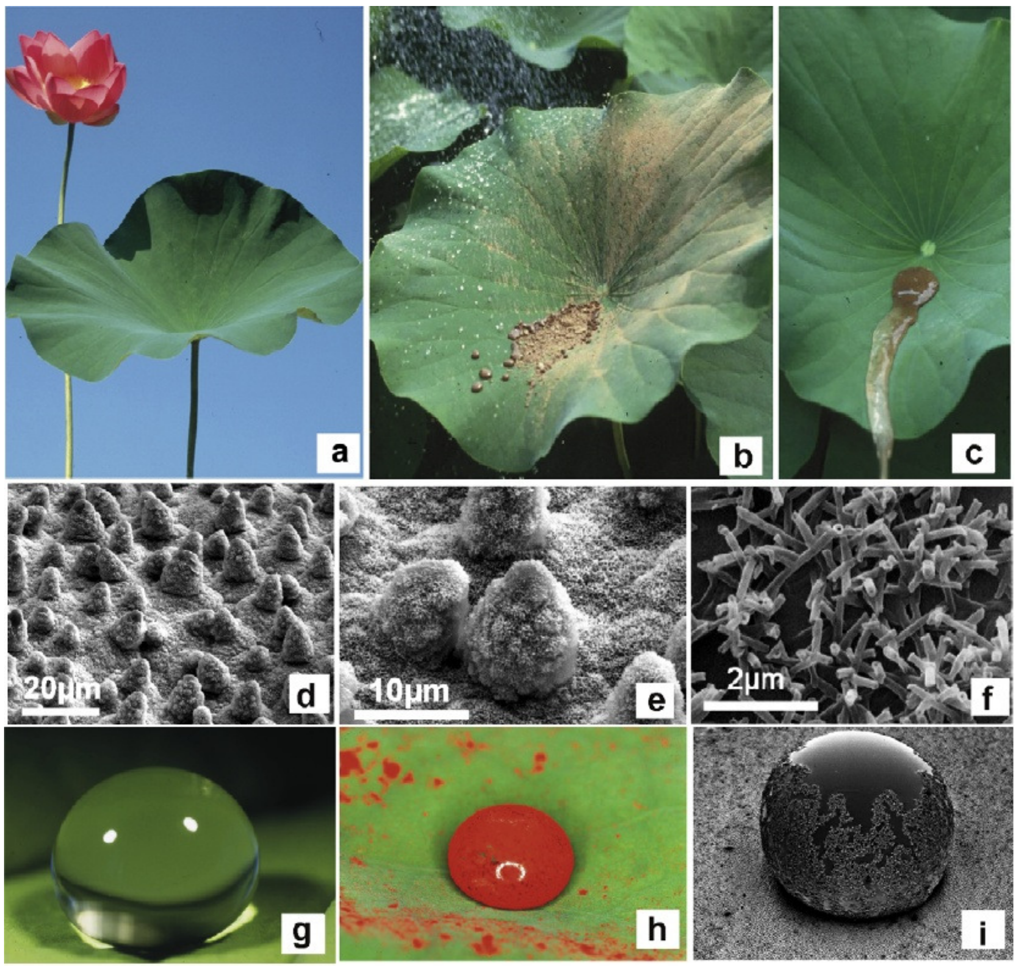

Figure 1-1: Superhydrophobic and self-cleaning lotus surface: a) a flowering plant of lotus; b, c) self cleaning with water; d, e, f) lotus leaf surface in different magnifications; g, h, i) superhydrophobicity of lotus leaf

A droplet of water that sits on a lotus leaf is forced to reduce its area of contact to the leaf because the leaf surface is hydrophobic. This means that the water droplet, rather than sticking onto the leaf, rolls off it. In addition, the resulting reduction in flow drag eases the removal of the contaminations from the leaf surface which becomes capable of self-cleaning its surface [4, 5]. The reason for this excellent surface property is found in the hierarchical roughness of the leaf incorporated with the presence of a hydrophobic wax coating [4-6]. Surface roughness brings about superhydrophobicity, self-cleaning and reduction of drag in fluid flow; each of these characteristics has already attracted the attention of engineers in various applications, including self-cleaning windows, exterior paints for buildings, ships and aircraft, roof tiles, textiles, solar panels [3].

Drag resistance skin of shark. Sharks can move in water at high speeds, with a low energy input [3]. The well-designed skin of shark turns out to be the major reason in reducing the drag on the animal body from fluid flow [7, 8]. A closer look at shark skin reveals very small tooth-like scales ribbed with longitudinal grooves (aligned parallel to the local flow direction of the water), which results in highly efficient water flow over the shark skin (Figure 1-2a) [3]. Textile engineers have been inspired by the structural design of the shark skin to produce a new generation of swimming suits with extremely low drag coefficients (Figure 1-2b) [9].

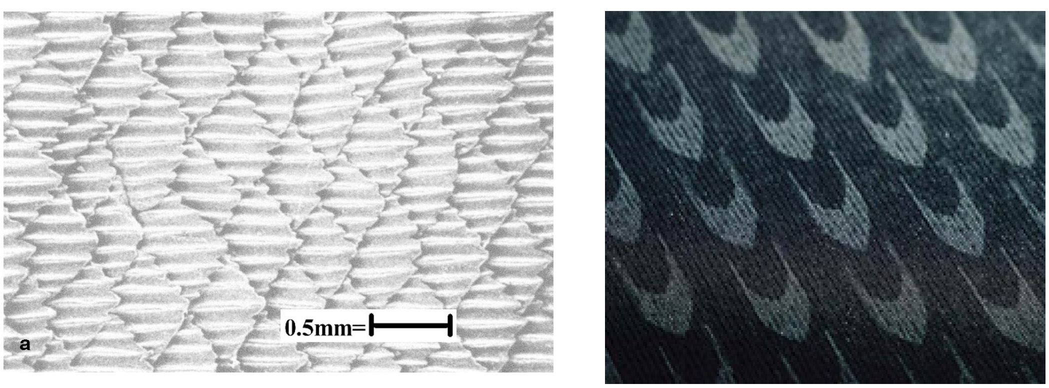

a) **b)**

Figure 1-2: Shark skin: a) Silky shark skin photograph [10]; b) swimming suit mimicking shark skin produced by Speedo [11]

Thermal sensitivity of beetles. The Melanophila beetle is a unique insect that has the ability of detecting fire from kilometers away. A special infrared organ embedded in its body can detect the infrared radiation emitted from fire. The beetle seeks the burnt trees because they provide good environment for development of its larvae [12]. The thermal sensitivity of beetles and the related mechanisms involved in this phenomenon has generated interest in researchers, who are willing to develop infrared sensors with application to smoke and heat detection [3, 12, 13].

There is a remarkable difference between design in nature and design in engineering. There is no doubt that nature has a limited range of available material and has to build the structures out of these materials; in contrast, engineering materials exist in a vast variety. In addition, biological structures have evolved to survive in their environmental conditions where the change in temperature is not very high and the mechanical loadings are confined to the natural ambient in which they grow. The questions that inevitably arise when we examine nature are: Are the biological systems optimized? How can we learn from nature to design artificial devices?

Nature uses very sophisticated processes and mechanisms to grow biological materials and structures with excellent mechanical performance from relatively weak materials. Biomimetics is a discipline useful at all design stages because several lessons can be learned from the architecture of biological structures. A designer can mimic the biological mechanisms and processes to design novel materials and structures by using engineering materials that have enhanced properties and performances for a wide range of temperature and mechanical loading. Therefore, biology can be an excellent source of inspiration for artificial syntheses [14].

Biological structures resort to particular mechanisms to grow themselves in such a fashion that they adapt optimally to their living conditions. During the process of adaptive growth [15], for example, a tree grows its structure to minimize stress concentration and achieve a uniform stress distribution. Consistent with the source of the external load, biological structures intensify their growth in regions subjected to overload. As a result, the stress is distributed in a larger area where more uniform stress appears [15, 16]. This phenomenon is observed in various natural structures such as trees, deer antlers, animal claws and etc [17].

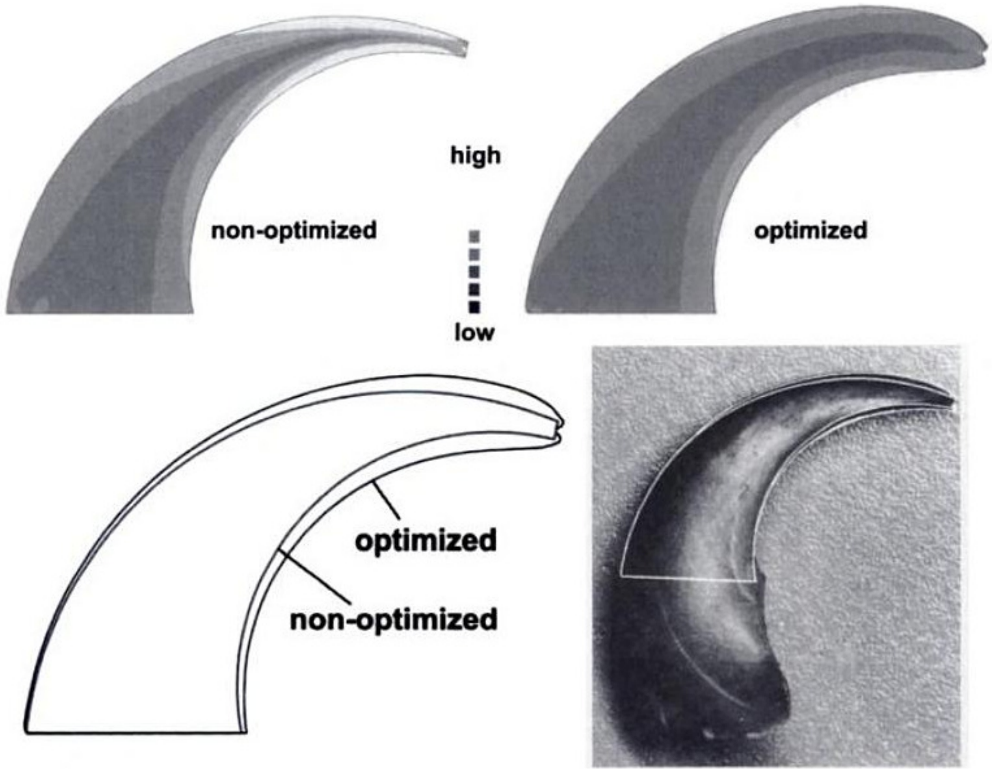

Figure 1-3: Optimization study on tiger claw

To prove the hypothesis that biological structures optimize themselves for carrying external loads, several optimization studies were carried out on different species. For instance, Mattheck et al. [18] used a Computer-Aided Optimization (CAO) strategy to investigate whether the tiger claw is optimally grown. Assuming the worst case of loading on the claw, which is a point load exerted at its tip, they found the optimum topology of the claw by analyzing its structure in a finite element package (Figure 1-3). He compared the optimized claw shape with the profile of an engineering-designed hook, which is a circle-shaped claw and found that the Von-Mises stress is uniformly distributed within the claw for its optimized profile whereas it is concentrated at the tip of the claw for the circle-shaped one. Therefore, the optimized real craw can withstand more severe loads.

Following a similar approach, the present study aims at discovering some of the design rules underlying the structure of gastropod shells. Seashells are hard biological structures that are believed to be optimally designed for protection against mechanical threats. As such, seashells are now considered a potential source of inspiration for biomimetics.

1.2 Mollusk Seashells

Mollusks are marine animals that have a very soft body [19]. Various dangerous factors, e.g., attacks from fishes or other predators or impact from a falling rock continuously threatens their soft tissues. Nature has wisely devised a suitable protection for mollusks in the form of a hard ceramic layer known as a seashell or simply a shell [2].

To this date, about 60,000 species of mollusk shells have been found in nature [20], with a great variety of shell sizes and shapes. Mollusk shells are categorized into several classes but most mollusk species fall within three main categories: bivalves, gastropods and cephalopods (Figure 1-4). Complicated spiral-like shapes are found in cephalopod class whereas bivalve and gastropod shells possess simpler shapes.

a) b) c)

Figure 1-4: Examples of seashells: a) scallop (bivalve class); b) abalone (gastropod class); c) nautilus (cephalopod class)

Several attempts were made to capture the shapes of seashells using mathematical formulations [21-24]. In addition to shape, seashells exist in a variety of sizes starting from less than 1 mm (micromollusks) up to 25 cm in shell of abalone.

The strength of shells is a function of the shape and the size of the shell, and of the materials it is made of. Depending on the living environment of the mollusk shells, various types of loading may be applied on the shell structure. For instance, seashells are prone to an impact load from the falling of rocks, attacks from other marine animals such as sharks and crabs or hydrodynamics loads of high-energy environments [25]. The shell structure is adapted to that living condition to withstand feasible threats from nature. Excessive mechanical load will of course break the shell, following failure patterns which also depend on the structure and geometry of the shell. In the case of a sharp penetration, the shell may fracture only in a small region of the structure while the other parts remain intact. On the other hand, distributed loading may crush the shell into several pieces. Zuschin [25] performed numerous compressive and compaction experiments on three seashell species, i.e., Mercenaria mercenaria, Mytilus edulis and Anadara ovalis, to obtain their strength, failure pattern and the predictor parameter on the strength of the shell. Among all the structural and geometrical parameters of the shell, shell thickness was revealed to be the most significant predictor of the shell strength. He reported various failure patterns but all commonly led to break the shell into few pieces. In Figure 1-5 the failure patterns achieved for Anadara ovalis shell are shown.

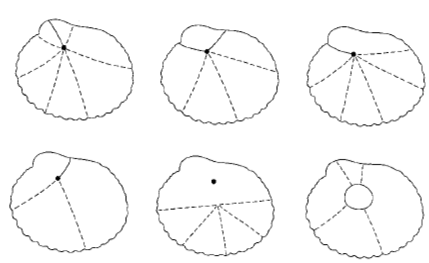

Figure 1-5: Schematic of failure patterns for Anadara ovalis seashell. Solid dot represents the loading point and dashed line depicts the failure crack [25].

Several factors can determine the failure pattern of the shell. Generally, failure starts from one region due to a high stress concentration and propagates toward other parts of the structure. Bending stresses, Hertzian contact stresses and delamination are possible causes of failure initiation depending on the type of the load and geometry of the shell. Shell bucking is another scenario where the whole structure collapses suddenly. For a given shell geometry and load, the shell structure can be analyzed to predict the mode of failure by which eventually the rupture pattern of the whole structure can be predicted. An interesting study on possible failure modes of a ceramic-based layer shell structure was accomplished by Lawn et al. [26], who observed various failure modes for different shell structures. For the case of a single-layer shell, flexural failure and Hetzian conical failure were observed (Figure 1-6) and in a two-layer shell, delamination was also recognized to be a feasible mode of failure.

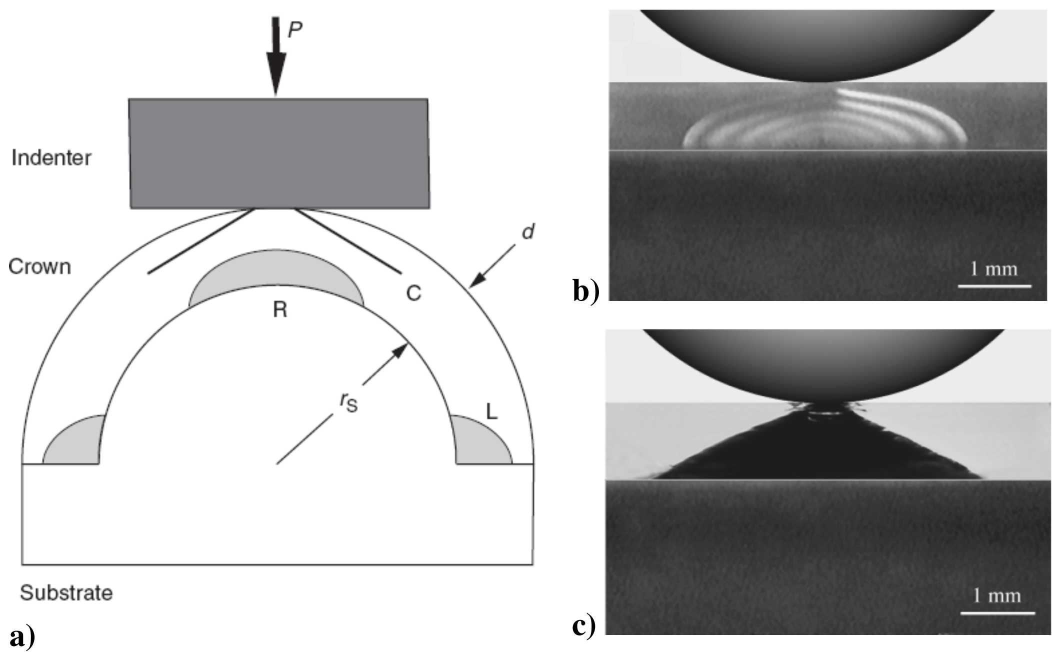

a)

b)

c)

Figure 1-6: Failure modes in a single layer ceramic shell: a) schematic of the shell and failure modes; b) flexural failure in inner surface of the shell; c) Hertzian conical crack initiated from top surface

Mollusk shells are composed of two distinct materials. The shell consists of calcium carbonate in the form of aragonite or calcite incorporated with an organic

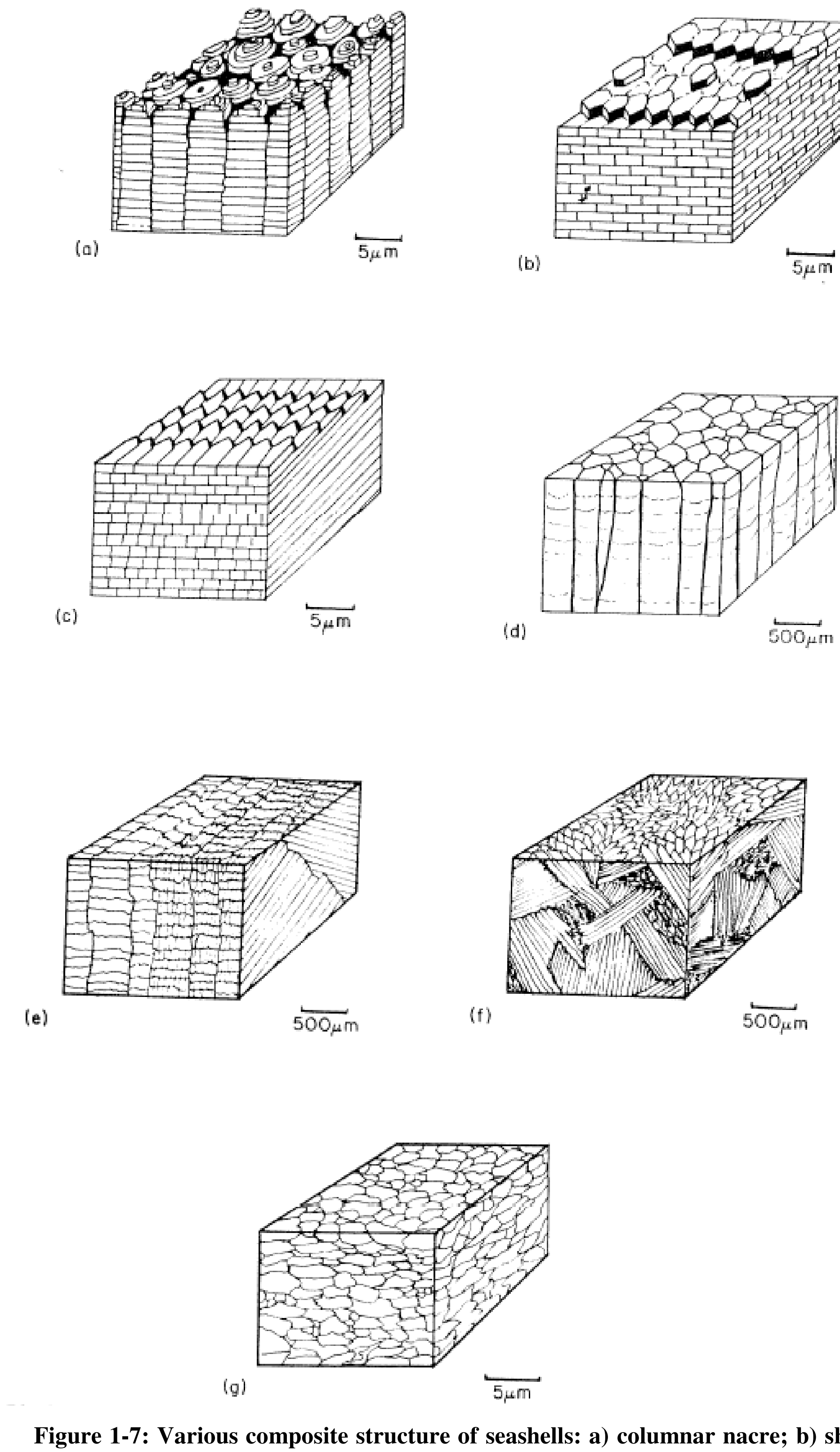

Figure 1-7: Various composite structure of seashells: a) columnar nacre; b) sheet nacre; c) foliated; d) prismatic; e) cross-lamellar; f) complex cross-lamellar; g) homogeneous [27]

material as a matrix, which never exceeds 5% of the total volume. These two ingredients can be arranged in a variety of combinations including prismatic, foliated, cross lamellar structure, columnar and sheet nacre (Figure 1-7)) [27]. Amongst all these seashell structures, nacreous structure appeared to have the highest tensile strength (120 MPa) for the shell Turbo. Nacre actually shows impressive mechanical properties: it is 3000 times tougher than bulk calcite [28] (Figure 1-8).

Nacre constitutes the inner layer of gastropod and bivalve seashells whereas their outer layer is composed of calcite. Calcite is a prismatic ceramic material made of calcium carbonate, ($CaCO_3$), which is a hard but brittle material. On the other hand, nacre forms the iridescent inner layer of the seashell. Nacre is a tough and ductile material, which shows relatively large plastic deformation prior to failure [28-30]. The combination of hard calcite layer with tough and stiff nacre is believed to be the ideal structure for protection of the mollusk animal [28, 29]. When a seashell is exposed to a concentrated load, for example a predator's bite, the hard ceramic layer is a suitable material for preventing penetration. Even if for any reason the calcite material fails, a crack initiates and starts to propagate toward the mollusk soft tissue. But when it reaches the interface of the two layers, tough nacreous layer delays the failure by preventing the crack propagation and complete failure of the shell. As a result, mollusk animal survives because of its excellently designed protective shell that prevents catastrophic rupture.

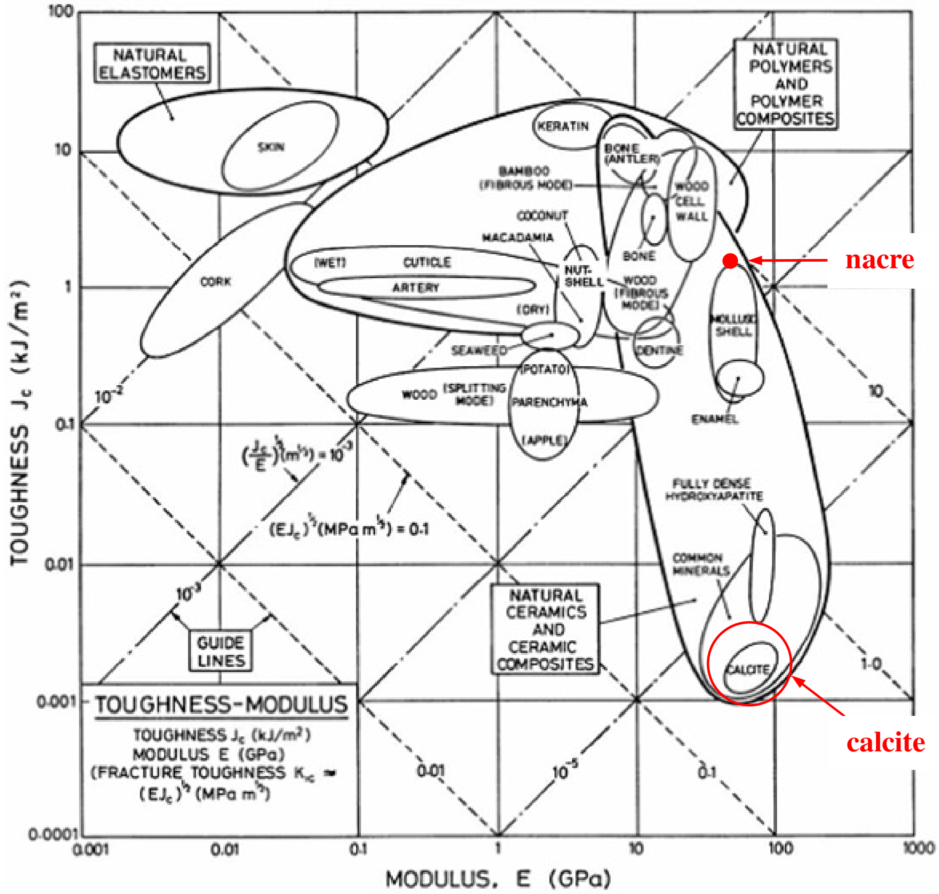

Figure 1-8: Toughness- Modulus chart for natural materials [31]

1.3 Calcite

Calcite is a polymorph of carbonate calcium, $CaCO_3$, which is a mineral ceramic material. It comprises a prismatic microstructure (Figure 1-9) whose prisms are organized normal to the surface of the shell to provide the calcite layer with the highest strength normal to the shell surface, which is good for resisting against indentation [32]. As a ceramic material, calcite is a hard but brittle material with radial cracks originating from the high stress concentration regions on the surface of the material and propagating in depth between the prisms [32]. Calcite prisms are about a few microns in edge and have an aspect ratio of about 5 [33]. Each prism is constructed from nanometer-sized grains with a diameter of about 32 nm [32].

Calcite possesses different strength along different orientations because of its prismatic structure. The experiments performed on the calcite of seashells of different classes revealed the variation in the strength along three orthotropic directions. Calcite from the Neverita Josephinia gastropod shell showed the lowest strength with a value of 70 MPa whereas calcite of the Perna Canaliculus bivalve shell was found to be the strongest with a maximum strength of about 182 MPa [34].

a) 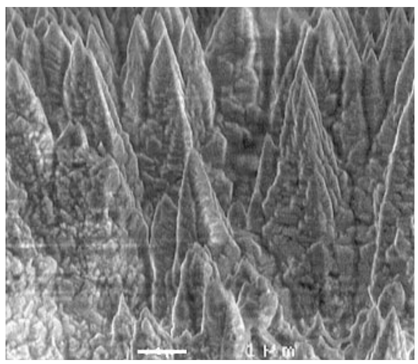

b) 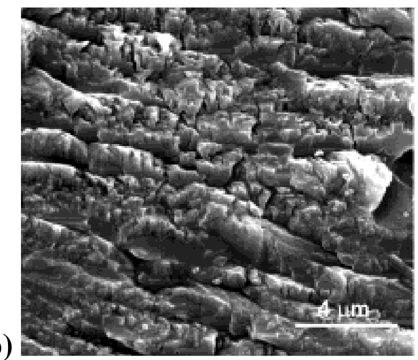

Figure 1-9: Prismatic structure of calcite: a) SEM image of scalenohedron calcite crystallites [35]; b) SEM image of the fracture surface of the prismatic calcite material [32].

1.4 Nacre

The hierarchical structure of nacre is believed to be the important key factor in giving nacre such striking mechanical properties. In a hierarchical structure, there are some promising features and mechanisms at different length scales, which make the overall structure well-designed [36]. Nacre, as a biological composite material, has several levels of hierarchy [28, 29] (Figure 1-10).

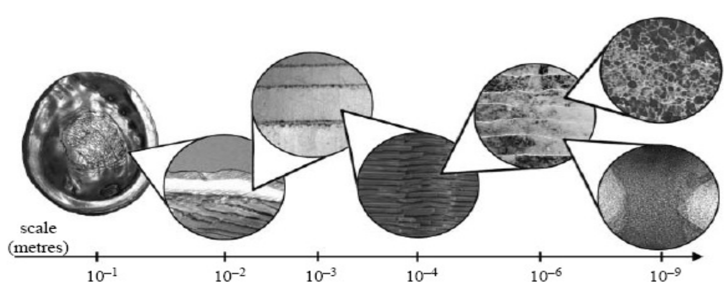

Figure 1-10: Hierarchical structure of nacre [2].

1.4.1 Microstructure of nacre

Microscopic imaging of nacre has revealed that nacre has an organized and well-designed microstructure. By cutting a cross section of nacre, a brick-wall micro-structure, sometimes referred as a brick and mortar structure [28], can be observed (Figure 1-11a). The “bricks” or “tablets” are separated by this soft organic material, which serves as a matrix. The organic matrix, which is composed of proteins and polysaccharides, comprises less than 5% of the volume of the nacreous composite. Hereafter, the inter-lamella distance is called interface and the inter-tablet gap is referred as junction [29] (Figure 1-11b).

Tablet size varies from a seashell to another. In the nacre of a mature red abalone, the average diameter ranges from 5 to 8 μm and tablet thickness varies from 0.2 to 0.9 μm. The thickness of organic interface was found to be about 20 to 30 nm, being small compared to that of a single tablet [29, 30, 37].

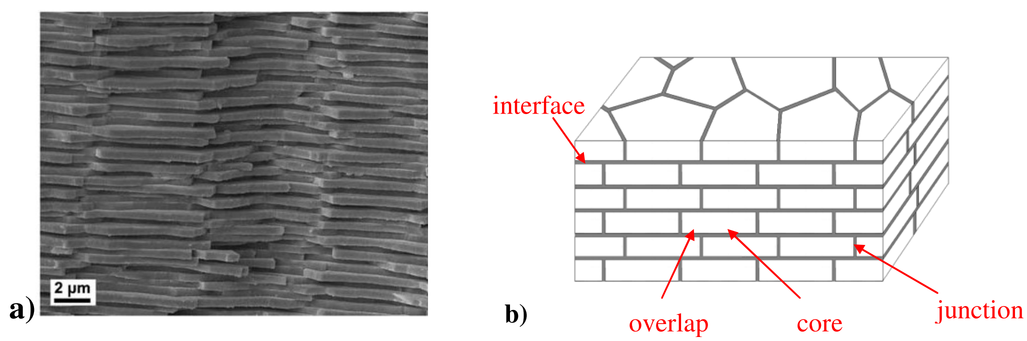

Figure 1-11: Microstructure of nacre: a) scanning electron micrograph of a fracture surface in nacre [29]; b) schematic of tablet arrangement in nacre

Tablets in neighbouring layers are arranged in two distinct regions, the “overlap” and “core”. The “overlap” is the region where two adjacent tablets overlap with each other (Figure 1-11b). The remaining part of each tablet, which is not covered in the overlapping region, is referred as the “core” [29]. Columnar and sheet nacre differ in their microstructure, i.e., the overlap configuration (Figure 1-12). In columnar nacre, tablets from adjacent layers are stacked in columns to achieve a regular pattern through the overall structure. In sheet nacre the tablets are arranged randomly within the layers and an irregular tablet configuration emerges among layers [29, 37, 38].

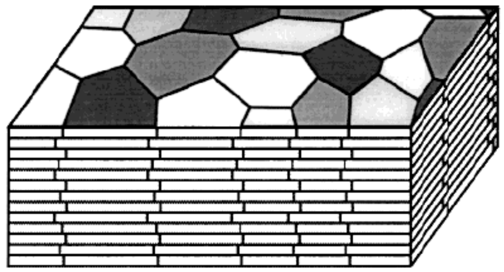

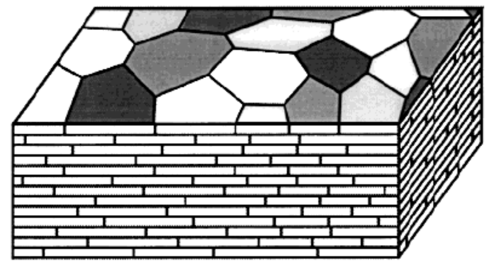

a) b)

Figure 1-12: Schematic demonstration of nacreous structures: a) columnar nacre; b) sheet nacre [37]

The overlap region in columnar nacre covers around 1/3 of the area of a tablet, whereas in sheet nacre half of each tablet is overlaid. Generally, the columnar nacre is found in highly curved shells such as red abalone, whereas the sheet nacre occurs more in flatter shells like pearl oyster [39].

By looking deeper at the microstructure of nacre, it was observed that the tablets are wavy (Figure 1-13a), contributing to energy dissipation [29]. Furthermore, mineral bridges between the tablets of adjacent layers were recognized to also play a role in energy dissipation (Figure 1-13b). Mineral bridges form during the growth of the shell and contribute to the biomineralization process. During this process, first an organic sheet emerges on the top of an existing layer. Then, the mineral bridges nucleate on the surface of the underlying tablets and grow vertically until they hit the organic interlamella sheet; finally, they grow laterally to generate the new tablet layer [40-42].

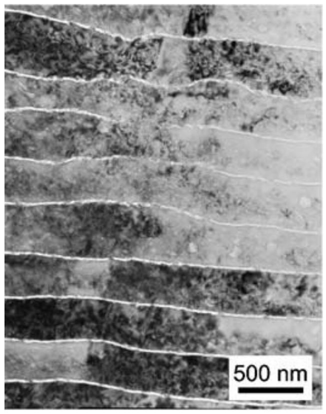

a)

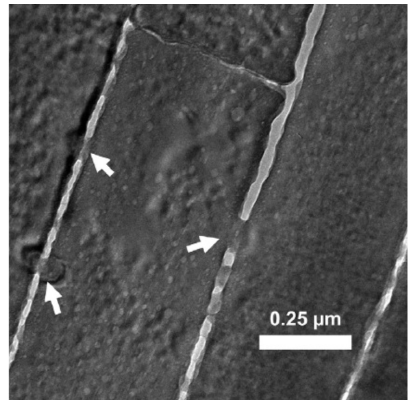

b)

Figure 1-13: Transmission electron micrograph of nacre: a) tablet waviness [29]; b) mineral bridges between tablets of neighboring layers shown by arrows [41]

1.4.2 Mechanical properties of nacre

Numerous experiments have been performed on nacre of different seashells to characterize their mechanical properties. Jackson et al. [43] performed experiments on nacre of Pinctada shell, which is a bivalve mollusk. The results of three-point bending experiments showed that the Young's modulus of nacre was 60 GPa for wet and 70 GPa for dry nacre. Barthelat et al. also characterized the elastic modulus of red abalone nacre by doing tensile test on dog-bone specimens. They revealed the elastic modulus of 90 and 70 GPa for dry and wet nacre, respectively.

The three point bending experiments on specimens of different seashell classes with distinct microstructure revealed that the tensile strength of different seashell species varies from 56 MPa to 116 MPa and nacreous seashells exhibit higher strength compared to others [39]. Doing the same type of experiment, Wang et al. [37] characterized the flexural tensile strength of red abalone and pearl oyster nacre and respectively obtained values of 223 and 227 MPa for loading (in flexure) parallel to the surface plane. The same experiment, but perpendicular to the tablet lamella, revealed flexural strength of 194 and 248 MPa for red abalone and pearl oyster nacre, respectively. From the results of tensile tests on dumbbell specimens of nacre by Jackson et al. [43], the tensile strength of nacre was determined to be 140 MPa and 170 MPa for wet and dry nacre, respectively. Barthelat et al. [29] observed that dry nacre in tension behaved like a brittle monolithic ceramic material with average failure strength of 115 MPa. In contrast, hydrated nacre exhibited inelastic deformation after a stress of 70 MPa was exceeded. Failure occurred at a strain of 0.01, which is significant compared to the nacre brittle constituents. Sarikaya et al. [44-46] continued carrying out mechanical tests on nacre of red abalone (*Haliotis rufescens*) and obtained a fracture strength of 185 ± 20 MPa (in bending tests).

Menig et al. [47] conducted compression tests on nacre specimens cut from red abalone. The compressive strength of wet nacre reached to 235 MPa with layers of tablets parallel to the loading direction and 540 MPa for loading direction perpendicular to the surface of tablets.

Shear tests were also performed by Barthelat et al. [29] to investigate the shear response in wet and dry nacre. Both dry and wet nacre showed an inelastic shear deformation and hardening after an initial linear elastic response, with shear modulus values of 10 and 14 GPa for wet and dry nacre, respectively. Yielding shear stresses for wet and dry nacre were respectively claimed to be 20 and 55 MPa. In wet nacre, rupture took place at shear strain of about 0.15, which is again surprisingly high for such a composite material with moderate components. Menig et al. [47] also tested nacre in shear for the case that the layers of tablets were parallel to the direction of the shearing force and found the maximum tensile strength of nacre as 29± 7.1 MPa.

The experiments by Jackson et al. [43] also revealed that the work of fracture of nacre varies from 350 to 1240 J/m^2, depending on the degree of hydration and span to depth ratio (an experimental parameter in three point bending). Surprisingly, the work of fracture of nacre was found to be 3000 times greater than that of pure ceramics. Fracture toughness of $8 \pm 3\,\mathrm{MPa}.\sqrt{\mathrm{m}}$ was also reported for nacre

[44-46]. The average values of fracture toughness and fracture strength of nacre were up to 20-30 times higher than those of a pure calcite.

1.4.3 Deformation and toughening mechanisms of nacre

Results obtained from different experiments motivated researchers to investigate the source of large plastic deformation and the corresponding toughening mechanisms. It seems that the shearing of the interface and the sliding of the inorganic tablets on one another is the key mechanism of inelastic deformations [28, 37, 43, 48]. The nanometer size of the mineral crystals in nacre is suggested to be a source of toughening and crack resistance [39, 49]. Sarikaya et al. [45, 46] proposed several toughening mechanisms: (a) crack blunting/branching/deflection, (b) microcrack formation, (c) plate pull out, (d) crack bridging (ligament formation). Nanoasperities on the surface of the mineral tablet were also discussed as a cause of strengthening the nacreous composite. [37, 50, 51]. In addition, the mineral bridges across the interfaces are also known as a toughening and strengthening feature in nacre [52]. Barthelat et al. proposed that the waviness of the tablet influences the hardening and damage tolerance behaviour of nacre [29].

In order to validate the predictions about the microstructure of nacre, some finite element studies were carried out. Katti et al. [53, 54] developed a three-dimensional FEM model to simulate the deformation mechanism of nacre. The effect of the aspect ratio of tablet was analyzed by doing a parametric study in FEM [55]. Nanoasperities on the tablets were also taken into consideration to capture their contribution in the performance of nacre [51, 56]. Further three-dimensional finite element modeling was used by Barthelat et al. [29] to study the effect of tablet waviness. The influence of the organic matrix Poisson's ratio on the stress distribution on the nacreous biocomposite and corresponding elastic modulus were also examined via a two-dimensional finite element model [57, 58]. In addition, the hardening effect of mineral bridges was taken into consideration within the core region to explore their effect on the elastic properties of nacre. As a result, it was found that the mineral bridges do not affect the in-plane elastic modulus of nacre, as was expected before, because the stress transfer occurs in the overlap region where there is no mineral bridge. However, the mineral bridges reinforce the composite in transverse tension and shear since the effect of stiff mineral bridges appear in the stress transfer mechanism, where an improvement in the consequent elastic properties was achieved [58].

In addition to the finite element modeling, mathematical models were developed to reproduce the stress transfer and mechanical properties of nacre. Gao et al. [49] presented a solution for the elastic modulus of nacre. A more detailed analysis was carried out by Kotha et al. [59] who studied the elastic and plastic deformation of nacre. They assumed a representative volume element of the nacre microstructure for the case of the fully overlapped nacre. However, their model could not simulate the whole plastic deformation observed in the experiments. Assuming a simple two-dimensional micromechanical model, Bertoldi et al. [60] formulated the mechanical properties of nacre as an orthotropic material. The outcome of their work was presented as a closed form solution to evaluate the macroscopic performance of nacre according to its microscale constituents; however, their solution did not agree with the experimental data.

All the discussed mechanisms have predicted some features about the responsible toughening and strengthening mechanisms of nacre. Several attempts were made to simulate the mechanical behaviour of nacre by employing finite element analysis. In addition, artificial composites were synthesized at macroscale from different materials mimicking some features of the microstructure of nacre [61-65]. Although there have been some improvements in the mechanical properties, artificial composites cannot, to this day, reproduce the degree of mechanical performance of nacre. The inconsistencies between the experimental results on nacre and those of numerical solutions or artificial composites are due to the fact that to this date, the exact mechanism which makes nacre a high-performance structure, has not been found [14].

1.5 Thesis Objectives

Is a seashell optimally designed over several length scales? How does it utilize two layers of distinct materials for the protection of the mollusk animal? Can we learn from the structure of the seashell to design artificial shells? These are the questions that we try to answer in this thesis. The main goal of this thesis is to investigate the relationship between the structure of the seashell and the material properties of its constituents. This is done by modeling the geometry of the shell in a finite element package and analyzing its mechanical behavior prior to failure. As a multiscale study, the structure of the shell is modeled at the macroscale, whereas the material properties of nacre are controlled at the microscale. Using this approach, we aim at coupling the influence of two scales to investigate the hierarchical structure of the seashell, which grows in an optimal fashion to resist natural dangers.

At the microscale, a closed form model of the in-plane modulus of nacre proposed by Kotha et al. has been modified to include the effect of the overlap and the junction between tablets. A failure criterion has also has formulated to predict the failure of nacre subject to multiaxial tensile stresses.

Eventually, by applying several optimization techniques, we intend to indentify the strongest seashell structure against a sharp penetration. By this investigation, we aim to find the relationship between the natural seashell and the optimized one to perceive how nature optimizes the seashell structure and material. The performance of the seashell at the onset of failure and the way it ruptures is of interest. On the other hand, by performing experiments on the actual seashells and observing their behavior at failure, we try to validate the optimization results. As a result of this investigation, a design guideline for designing two-layer shells will be finally proposed to improve the performance of man-made protective armors undergoing similar structural and loading conditions.

1.6 Thesis Structure

The thesis is organized into 6 chapters. Chapter two describes the closed form models formulated for the microstructure of nacre. The procedures for developing the in-plane elastic modulus and deriving the multiaxial failure criterion for nacre are explained. Chapter three gives explains the macroscale finite element model of the seashell and the possible modes of failure. Chapter four presents the optimization techniques that are employed to obtain the strongest shell. Chapter five discusses the results of experiments accomplished on actual samples of red abalone seashell. Finally, chapter six summarizes the main features of this thesis and proposes a guideline for the design of a two-layer shell.

Chapter II Microscale Modeling

The mechanical properties of calcite and nacre are needed to model the shell at the macroscopic scale. Here calcite was assumed to be homogenous, isotropic, linear elastic and brittle [66]. Nacre, which is a more complex material, was assigned material properties that were dependant on its microstructure.

Nacre is transversely isotropic, i.e., in the plane of the tablets and out of the plane of the tablets [29, 43]. Furthermore, the choice of an appropriate failure criterion is required to suitably predict the failure of nacre under various loading conditions. This chapter presents a representative volume element (RVE) based on the microstructure of nacre. The mechanical properties of nacre along different directions are computed using this RVE. In addition, a failure criterion for multiaxial tensile state of stress is proposed to predict the failure of nacre under different tensile stresses.

2.1 Representative Volume Element

A subset of a material's microstructure, which can represent the mechanical behavior of the bulk material, is called a representative volume element (RVE). The RVE was defined by Kanit [67] as a volume of heterogeneous material that is sufficiently large to be statistically representative of the composite, i.e., to effectively include a sampling of all microstructural heterogeneities that occur in the composite. The use of RVE leads to a remarkable reduction in the computation size whereas the results are generalized for the overall configuration. Based on the microstructure of nacre, a RVE is proposed in Figure 2-1.

In the RVE, t_i and t_t represent the thickness of interface and tablet, respectively, whereas L_t is the length of the tablet. The region where two tablets from two adjacent layers overlap is called "overlap", as shown by l_o. It should be noted that the overlap length varies according to the type of nacreous seashell. For instance,

l_o represents half of the tablet length in pearl oyster and 20% of the tablet length in red abalone [29]. σ_{xx}, σ_{yy} and τ_{xy} are the axial stress along the tablet, the normal stress across the tablet and the corresponding shear stress, respectively.

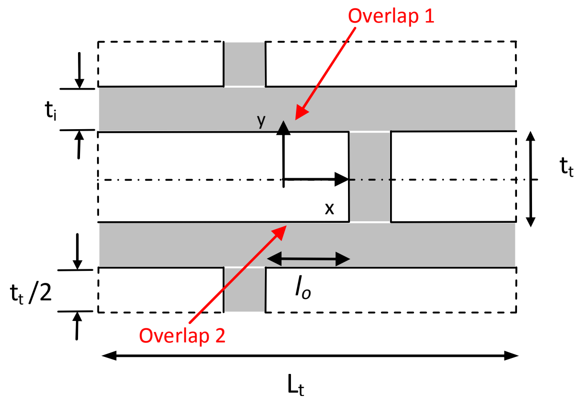

Figure 2-1: Schematic of representative volume element

For the RVE, the following assumptions are hold:

- Tablets have uniform thickness. In the plane of tablets, they have squared cross section.
- Axial stresses along the tablets are carried through the tablets while the interfaces only transfer shear stresses.
- Axial and shear stresses are assumed to be uniform across tablets and interface.
- Stresses along *y* and *z* axes are ignored.
- Plane stress condition is considered in the calculations because the tablets have finite dimensions and the soft organic interface makes the *x*-*y* and *x*-*z* surfaces of the tablets to behave as free surfaces. As a result, the effect of Poisson's ratio is neglected.
- Periodic boundary conditions are ascribed to the RVE. Since

This RVE is used as a basic model to derive the failure criterion and improve the existing analytical formulation of the elastic modulus of nacre as described in the next sections.

2.2 In-Plane Elastic Modulus

An analytical solution of the in-plane elastic modulus of nacre was proposed by Kotha et al. [59]. In that model, the solution for fully overlapped nacre was developed neglecting the effect of junctions between two adjacent tablets of one layer. Since the overlap region transfers axial stress between the tablets, its length plays an important role on the total stress transfer as well as on the elastic modulus. Using the mentioned RVE, the analytical solution is improved here to include the effect of overlap's length. The effect of the junctions is also considered to model the whole microstructure of nacre in the formulation.

The following describes the procedure to derive the in-plane modulus in the scenarios where the effect of junction is either included or neglected.

2.2.1 In-plane modulus without the effect of junction

Due to the symmetry of the RVE about the horizontal axis (Figure 2-1), only one half of the whole RVE is actually modeled, as shown in Figure 2-2a. Subscripts 1, 2 and 3 stand for the properties of tablet 1, tablet 2 and interface respectively. In this part, the effect of junction is neglected, meaning that the ends of the tablets are free surfaces.

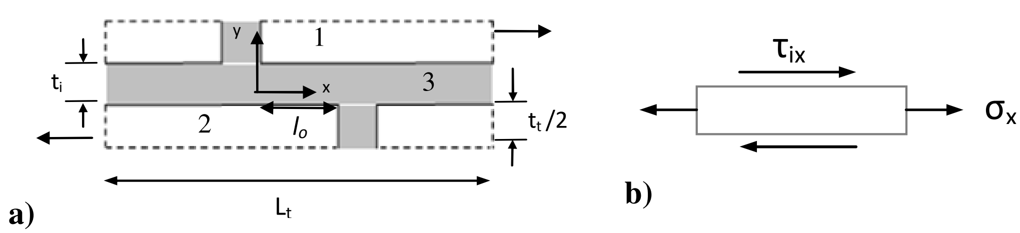

Figure 2-2: a) Part of RVE assumed as a unit cell for stress analysis of overlap; b) stresses applied on a tablet (The interface between the two layers of tablets and the junction between two adjacent tablets are out of scale to show their role in stress transfer)

Formulation of in-plane elastic modulus for the overall RVE involves first the analysis of stress transfer within the core and the overlap region. Then, the results for two regions are combined to formulate the elastic modulus. We start to focus on the overlap and calculate the stress and strain relations within that region.

The first equilibrium equation for the stresses on the tablets is:

$$\frac{\partial \sigma_x}{\partial x}+\frac{\partial \tau_{ix}}{\partial y}=0 \tag{2-1}$$

where σ_x is the axial stress in the tablet and τ_{ix} is the shear stress transferred from tablet to tablet by the organic interface (Figure 2-2b). Since it is assumed that the stress along the thickness of the tablet is uniform, integrating Equation 2-1over the thickness of the half tablet gives

$$\frac{d\sigma_{1x}}{dx}=\frac{\tau_{ix}}{t_t/2} \tag{2-2}$$

and

$$\frac{d\sigma_{2x}}{dx}=-\frac{\tau_{ix}}{t_t/2} \tag{2-3}$$

The negative sign in front of Equation 2-3 is due to the fact that in tablet 1 the axial stress is increasing along *x*-axis and vice versa, in tablet 2 the axial stress is decreasing. Summation of the stresses of two tablets at any point along *x*-axis is constant and equal to σ_o.

$$\sigma_{1x}+\sigma_{2x}=\sigma_o \tag{2-4}$$

On the other hand, the displacements of two tablets are related to the shear deformation of the interface following:

$$u_{1,x}-u_{2,x}=t_i\gamma_{ix} \tag{2-5}$$

where $u_{1,x}$and $u_{2,x}$ are respectively the displacements of tablet 1 and tablet 2 along the direction of *x*-axis and γ_{ix} is the corresponding interface shear strain in x direction. By differentiating Equation 2-5 with respect to x, we can write

$$\varepsilon_{1x}-\varepsilon_{2x}=t_i\frac{d\gamma_{ix}}{dx} \tag{2-6}$$

Using Hooke's law for replacing strains with stresses, Equation 2-6 changes to

$$\frac{\sigma_{1x}}{E_t} - \frac{\sigma_{2x}}{E_t} = \frac{t_i}{G_i}\frac{d\tau_{ix}}{dx} \tag{2-7}$$

where E_t is the elastic modulus of the tablet. Substituting Equations 2-2, and 2-4 into Equation 2-7, gives

$$\frac{d^2\sigma_{1x}}{dx^2} - \frac{4G_i}{t_t t_i E_t}\sigma_{1x} = -\frac{2G_i\sigma_o}{t_t t_i E_t} \tag{2-8}$$

where G_i is the shear modulus of the interface. Solving the differential equation of Equation 2-8 gives the general solution in the form:

$$\sigma_{1x} = \frac{\sigma_o}{2} + A\cosh(\alpha x) + B\sinh(\alpha x) \tag{2-9}$$

where A and B are constants which should be determined by the boundary conditions and

$$\alpha = \sqrt{\frac{4G_i}{t_t t_i E_t}}$$

The following boundary conditions are considered for the tablet 1

$$\begin{aligned} x = 0 &\Rightarrow \sigma_{1x} = 0 \\ x = l_o &\Rightarrow \sigma_{1x} = \sigma_o \end{aligned} \tag{2-10}$$

Applying the boundary conditions to Equation 2-10, yields

$$A = -\frac{\sigma_o}{2} \text{ and } \mathrm{B} = \frac{\sigma_o}{2}\frac{1+\cosh(\alpha l_o)}{\sinh(\alpha l_o)} \tag{2-11}$$

Substituting Equation 2-9 into Equations 2-2 and 2-4, gives the shear stress on the tablets and the axial stress in the tablet 2:

$$\begin{cases} \tau_{ix} = \dfrac{t_t\alpha}{2}(A\sinh(\alpha x) + B\cosh(\alpha x)) \\ \sigma_{2x} = \dfrac{\sigma_o}{2} - A\cosh(\alpha x) - B\sinh(\alpha x) \end{cases} \tag{2-12}$$

By integrating Equation 2-9 over the length of the overlap to find the average axial stress in the overlap region of tablet 1, one finds:

$$\overline{\sigma_{1x}} = \frac{1}{l_o}\int_0^{l_o}\sigma_{1x}dx = \frac{\sigma_o}{2} \tag{2-13}$$

The same procedure is followed for the core region to calculate stress and strain relations assuming that the axial stress is increasing in the tablet 1 along *x*-axis and is decreasing in tablet 2 (Equation 2-14). In the analysis of the core region, "prime" symbol is used to distinguish between the notation of the overlap and the core (Figure 2-3).

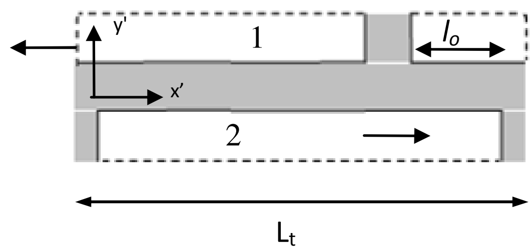

Figure 2-3: Part of RVE assumed as unit cell for stress analysis of core

$$\begin{cases} \dfrac{d\sigma'_{1x}}{dx} = -\dfrac{\tau'_{ix}}{t_t/2} \\ \dfrac{d\sigma'_{2x}}{dx} = \dfrac{\tau'_{ix}}{t_t/2} \end{cases} \tag{2-14}$$

The boundary conditions for the core region are different from those of the overlap

$$\begin{aligned} x' = 0 &\Rightarrow \sigma'_{1x} = \sigma_o \\ x' = L_t - l_o &\Rightarrow \sigma'_{1x} = 0 \end{aligned} \tag{2-15}$$

Following the same procedure for the core as it was done for the overlap and also using new boundary conditions (Equation 2-15), one can obtain the stress distribution within the tablets and the interface as

$$\begin{cases} \sigma'_{1x} = \dfrac{\sigma_o}{2} + C\cosh(\alpha x') + D\sinh(\alpha x') \\ \sigma'_{2x} = \dfrac{\sigma_o}{2} - C\cosh(\alpha x') - D\sinh(\alpha x') \\ \tau'_{ix} = -\dfrac{t_t\alpha}{2}(C\sinh(\alpha x') + D\cosh(\alpha x')) \end{cases} \tag{2-16}$$

where α is the same as defined before, and C and D are found by applying the boundary conditions

$$C = \frac{\sigma_o}{2} \text{ and } D = -\frac{\sigma_o}{2}\frac{1+\cosh(\alpha(L_t - l_o))}{\sinh(\alpha(L_t - l_o))} \qquad (2\text{-}17)$$

The average stress in the core region of two tablets can be computed as

$$\begin{aligned} \overline{\sigma'_{1x}} &= \frac{1}{L_t - l_o}\int_0^{L_t - l_o} \sigma'_{1x} dx' = \frac{\sigma_o}{2} \\ \overline{\sigma'_{2x}} &= \frac{1}{L_t - l_o}\int_0^{L_t - l_o} \sigma'_{2x} dx' = \frac{\sigma_o}{2} \end{aligned} \qquad (2\text{-}18)$$

Having found the stresses within the overlap and the core, we can proceed to calculate the elastic modulus of the RVE. The stress that the RVE can carry is proportional to the volume fraction of the tablets.

$$\sigma_{RVE} = (\overline{\sigma_{1x}})V_{1x} + (\overline{\sigma_{2x}})V_{2x} \qquad (2\text{-}19)$$

where V_{1x} and V_{2x} are the volume fraction of the tablet 1 and tablet 2 respectively. Replacing the values of average stresses for the two tablet gives

$$\sigma_{RVE} = \frac{\mathrm{t}_t}{\mathrm{t}_t + \mathrm{t}_i}\frac{\sigma_o}{2} \qquad (2\text{-}20)$$

To formulate the strain of the RVE, the displacement between two points, which have analogous position within the structure are calculated first and then the displacement is divided by the length of the RVE. Figure 2-4 depicts the path chosen to calculate the displacement between point A and B. The two different coordinate systems, which were used for the stress analysis of the overlap and the core, are shown in Figure 2-4.

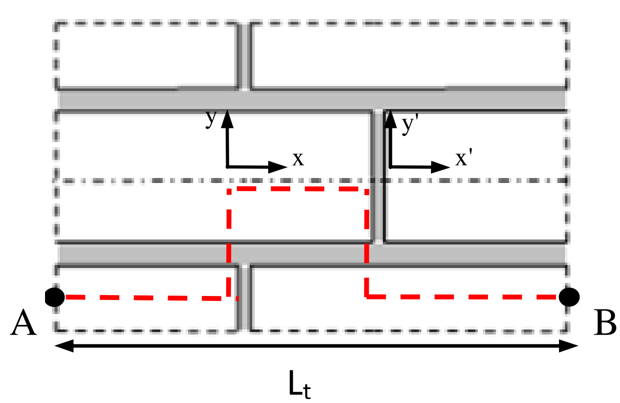

Figure 2-4: Selected path for calculating the strain

Therefore, the displacement between the point A and B can be written as

$$u_{A-B} = \overline{\sigma_{1x}}\frac{l_o}{E_t} + \tau_{ix}(\mathrm{x}=l_o)\frac{t_i}{G_i} + \tau'_{ix}(\mathrm{x}'=0)\frac{t_i}{G_i} + \overline{\sigma'_{1x}}\frac{L_t - l_o}{E_t} \qquad (2\text{-}21)$$

In Equation 2-21, the first and the fourth terms denote the displacement of the tablets 1 due to its deformation under axial stress while the second and the third terms represent the shear deformation of the interface at the end of the overlap and at the beginning of the core respectively.

Using Equations 2-12, 2-13, 2-16 and 2-18 in Equation 2-21 and dividing the result by the length of the tablet, the strain of the RVE can be obtained as

$$\varepsilon_{RVE} = \frac{\dfrac{\sigma_o}{2}\left[\dfrac{L_t}{E_t} + \dfrac{t_i t_t \alpha}{2G_i}\left(\dfrac{1+\cosh(\alpha l_o)}{\sinh(\alpha l_o)} + \dfrac{1+\cosh(\alpha(L_t - l_o))}{\sinh(\alpha(L_t - l_o))}\right)\right]}{L_t} \qquad (2\text{-}22)$$

The in-plane elastic modulus of the RVE can be determined by the general Hooke's law

$$E_{In-plane} = \frac{\sigma_{RVE}}{\varepsilon_{RVE}}$$

or

$$E_{In-plane} = \frac{\mathrm{t}_t}{\mathrm{t}_t + \mathrm{t}_i}\frac{1}{\left[\dfrac{1}{E_t} + \dfrac{t_i t_t \alpha}{2L_t G_i}\left(\dfrac{1+\cosh(\alpha l_o)}{\sinh(\alpha l_o)} + \dfrac{1+\cosh(\alpha(L_t - l_o))}{\sinh(\alpha(L_t - l_o))}\right)\right]} \qquad (2\text{-}23)$$

2.2.2 In-plane modulus with the effect of junction

In the previous section, the in-plane elastic modulus of nacre was obtained by neglecting the effect of junction in the stress transfer. In this section, the effect of junction is also incorporated with other stress transfer mechanisms. The same RVE as shown in Figure 2-1 is used assuming that the junction carries certain amount of stress shown by σ_{jun}, which is unknown and should be determined based on the necessary condition on the displacement of the organic material.

The same steps as the preceding section are used here with new boundary conditions to include the effect of junction. According to the initial assumption, the junction also contributes to the stress transfer rather than the organic interface; therefore, the stress at the end of the tablet is not zero. The boundary conditions for the overlap are

$$\begin{aligned} &x = 0 \ \Rightarrow \ \sigma_{1x} = \sigma_{jun} \\ &x = l_o \ \Rightarrow \ \sigma_{1x} = \sigma_o - \sigma_{jun} \end{aligned} \tag{2-24}$$

and those of the core are

$$\begin{aligned} &x' = 0 \ \Rightarrow \ \sigma'_{1x} = \sigma_o - \sigma_{jun} \\ &x' = L_t - l_o \ \Rightarrow \ \sigma'_{1x} = \sigma_{jun} \end{aligned} \tag{2-25}$$

Following the same steps described in the previous section, the stress distribution in the overlap region is obtained to be

$$\begin{cases} \sigma_{1x} = \dfrac{\sigma_o}{2} + A\cosh(\alpha x) + B\sinh(\alpha x) \\ \sigma_{2x} = \dfrac{\sigma_o}{2} - A\cosh(\alpha x) - B\sinh(\alpha x) \\ \tau_{ix} = \dfrac{t_t \alpha}{2}(A\sinh(\alpha x) + B\cosh(\alpha x)) \end{cases} \tag{2-26}$$

where

$$\alpha = \sqrt{\frac{4G_i}{t_t t_i E_t}}, \ A = \sigma_{jun} - \frac{\sigma_o}{2}, \ B = \frac{(\frac{\sigma_o}{2} - \sigma_{jun})(1 + \cosh(\alpha l_o))}{\sinh(\alpha l_o)}$$

and the stresses of the core region are

$$\begin{cases} \sigma'_{1x} = \dfrac{\sigma_o}{2} + C\cosh(\alpha x') + D\sinh(\alpha x') \\ \sigma'_{2x} = \dfrac{\sigma_o}{2} - C\cosh(\alpha x') - D\sinh(\alpha x') \\ \tau'_{ix} = -\dfrac{t_t \alpha}{2}(C\sinh(\alpha x') + D\cosh(\alpha x')) \end{cases} \tag{2-27}$$

where

$$\alpha = \sqrt{\frac{4G_i}{t_t t_i E_t}},\ C = \frac{\sigma_o}{2} - \sigma_{jun},\ D = \frac{(\sigma_{jun} - \frac{\sigma_o}{2})(1 + \cosh(\alpha(L_t - l_o)))}{\sinh(\alpha(L_t - l_o))}$$

Before calculating the elastic modulus, the unknown stress of the junction should be determined. By focusing on the intersection of the junction and the interface, a new boundary condition can be derived based on the continuity of the displacement at the junction and the interface (Figure 2-5a).

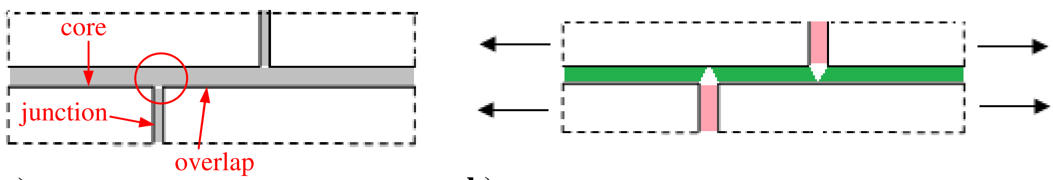

Figure 2-5: Schematic of organic interface a) in absence of external loading; b) deformed organic material when pulled by an axial load

When an axial stress is applied on the RVE, one portion of the loads is transferred via the junction and the rest is carried by the organic interface at the overlap of the two tablets in the form of shear stress. Hence, the displacement created by the organic material at the junction due to the axial stress should be equal to the one caused by the shear deformation of the interface at the end of the overlap and at the beginning of the core regions (Figure 2-5b).

$$\tau_{ix}(x = l_o)\frac{t_i}{G_i} + \tau'_{ix}(x' = 0)\frac{t_i}{G_i} = \frac{\sigma_{jun} t_j}{E_i} \tag{2-28}$$

where t_j and E_i are the thickness and the elastic modulus of the organic material at the junction respectively. Replacing Equations 2-26 and 2-27 into Equation 2-28 gives σ_{jun} in terms of σ_o, materials and geometrical properties of the RVE components.

$$\sigma_{jun} = \frac{N}{1+N}\frac{\sigma_o}{2} \tag{2-29}$$

where N is

$$N = (\frac{\alpha t_t t_i}{2t_j}\frac{E_i}{G_i})\left[\frac{1+\cosh(\alpha l_o)}{\sinh(\alpha l_o)} + \frac{1+\cosh(\alpha(L_t - l_o))}{\sinh(\alpha(L_t - l_o))}\right]$$

Finally, the elastic modulus can be written as

$$E_{In-plane} = \frac{\mathrm{t}_t}{\mathrm{t}_t + \mathrm{t}_i}\frac{1}{\left(\frac{1}{E_t} + \frac{t_j}{L_t E_i}\frac{N}{1+N}\right)} \tag{2-30}$$

2.2.3 Comparison of different in-plane moduli

In this section, the modified in-plane moduli of nacre are compared with Kotha's analytical solution. The thickness and length of the tablet is assumed to be 0.5 µm and 4µm respectively whereas the thickness of interface is assumed to be .028 µm [29]. The elastic modulus of aragonite tablets is fixed to be 100 GPa [66]. The shear and elastic moduli of the organic interface were set at 1.4 GPa and 2.84 GPa respectively, following experimental results [43]. It is assumed junctions and interfaces have the same thickness and mechanical properties.

In-plane elastic modulus relations are plotted as function of the overall length in Figure 2-6 from Kotha's model, and from the modified model with and without junctions. Nacre of different seashells have different overlap length and for the case of sheet nacre, the overlap covers 50% of tablet's length and in columnar nacre, 20% of tablet's length overlaps with the tablet in the adjacent layer.

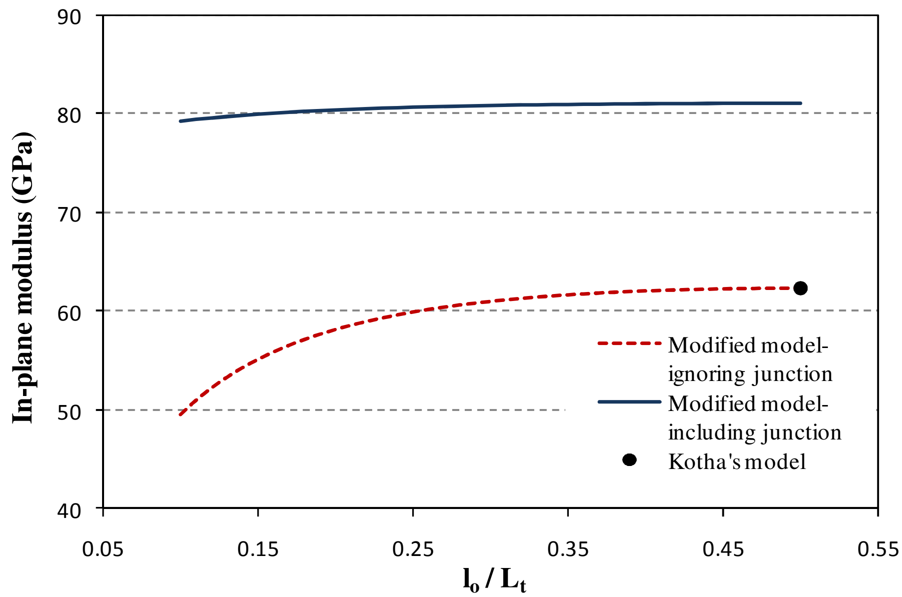

Figure 2-6: Comparison of different formulations for in-plane elastic modulus

As it can be observed from Figure 2-6, as the overlap length is decreased, the amount of the load transferred through shear in the overlap decreases and the elastic modulus decreases. Therefore, the assumption of the full overlap for modeling the elastic modulus of columnar nacre is not accurate enough and the new model should be considered. By taking the effect of junction into consideration, the modulus enhances remarkably, which was expected from before since the junction contributes to the stress transfer as well. However, the overlap shows less effect on the elastic modulus when the junction is considered. This is due to the fact that the junction transfers one portion of the total axial stress and the remaining portion is carried through the overlap. So, the intensity of the shear stress in the overlap reduces, which lessens the shear deformation of the organic interface.

2.2 Failure Criterion

Hydrated nacre, when tested in tension, shows significant inelastic deformation prior to failure. This large inelastic deformation, which brings about the high amount of energy absorption, is believed to be due to the tablet sliding [29, 37, 43]. When the shear stress in the organic interface exceeds its yield strength, it undergoes inelastic deformation making the tablets slide over one another until the maximum inelastic strain of the interfaces is reached and the whole structure fails (Figure 2-7). The examination of a fracture surface of nacre reveals that failure occurs along the interfaces [43]. Thus, the mechanical behavior of the interface is controlling the failure of nacre.

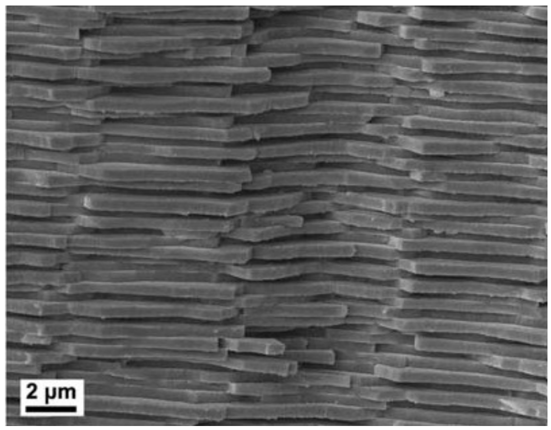

Figure 2-7: Fractured surface of nacre showing the occurrence of failure along the interfaces [29]

It was assumed that whenever any point of the RVE fails, the whole composite at macroscale collapses. This reasoning was first employed for predicting the failure of the composite material subject to the macroscale stresses by developing a micromechanical model that expresses all the possible failure mechanisms at microscale [68, 69]. Although conservative, this approach is appropriate to predict the failure of the total structure. The same reasoning was applied here to predict the failure of nacre subject to multiaxial tensile stresses.

In addition to the assumptions made in section 2-1for the RVE, the followings are also held to develop the failure criterion:

- The organic interface is isotropic in terms of strength, and its ultimate strength is the same in tension and shear.
- The failure of nacre occurs from the failure of the interfaces, which are the weakest components. When nacre is pulled out, the tablet sliding, which is

the key source of the large deformation in nacre, continues until the organic interface is not able to stretch more. At this point, the interface and consequently, the nacre fail [29, 37, 43].

- At the instant of failure, both interfaces and junctions are fully yielded so that the stress is distributed uniformly within these organic regions.

The basic idea to derive the failure criterion is to model the yielded interface with a series of parallel springs that can be stretched along and across the tablets (Figure 2-8).

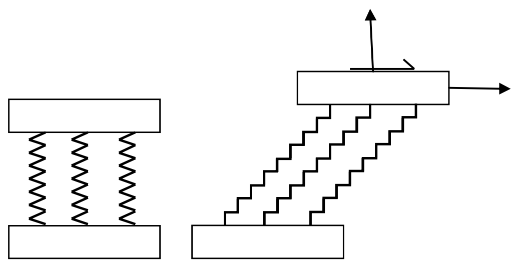

Figure 2-8: Organic interface replaced with a series of springs

The springs can stretch along and across the tablets orientation while they can carry a certain amount of the total force. In other words, there are two stress components on the organic material at the interface, i.e., shear and normal stresses (Figure 2-9). The combination of all these stresses can deform the springs to their limit, which is governed by the material properties of the organic material.
Shear stress can be applied on the interface by either direct transfer of RVE's external shear stress or axial stress along the tablet. As mentioned, if an axial stress parallel to the layers of tablet is applied on the RVE, it is transferred between tablets of adjacent layers in form of shear stress through the overlap region. On the other hand, when an external shear stress is applied on the RVE, it is transferred directly to the organic interface. Therefore, a combination of shear and normal stresses governs the net shear stress of the interface.

Transverse stress can be generated in the interface due to the normal stress across the tablet layers. When an external stress is applied on the RVE normal to the tablet direction, it is carried continuously through consecutive layers of tablets and interfaces.

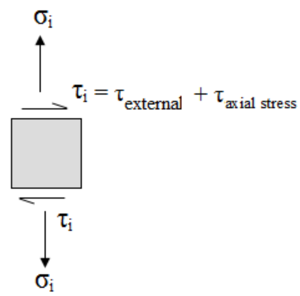

Figure 2-9: Various states of stresses applied on the organic interface in overlap

The following part describes the procedure for formulating the failure criterion.

If an external stress parallel to the plane of the tablets, σ_{xx}, is exerted on a piece of nacre, the stress at the end of the overlap of each tablet, σ', (Figure 2-10) can be written as

$$\sigma_{xx}(2t_t + 2t_i) = \sigma' t_t + \sigma_i^y t_t$$

or

$$\sigma' = \frac{\sigma_{xx}(2t_t + 2t_i) - \sigma_i^y t_t}{t_t} \tag{2-31}$$

where σ_i^y is the yield stress of the organic material, which is a constant material property with a value of 25 MPa [29].

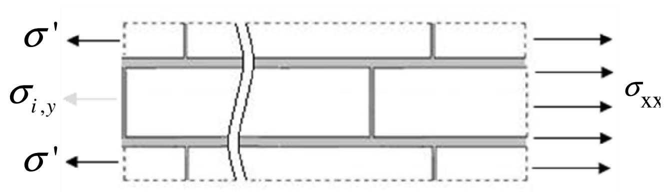

Figure 2-10: Stresses carried by the junction and tablet due to an axial stress

By assuming the overlap area of the tablet and by drawing its free body diagram (Figure 2-11), the stress equilibrium equation can be written

$$\sigma'(\frac{t_t}{2}) = \tau_{axial}(l_o) + \sigma_i^{\,y}(\frac{t_t}{2}) \tag{2-32}$$

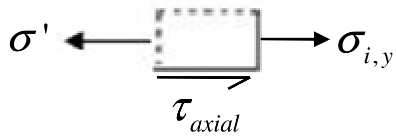

Figure 2-11: Free body diagram of the overlap region and corresponding stresses

Replacing Equation 2-31 into Equation 2-32, gives the shear stress produced in the overlap due to the axial stress

$$\tau_{axial} = \frac{\sigma_{xx}(t_t + t_i) - \sigma_i^{\,y}(t_t)}{l_o} \tag{2-33}$$

As previously discussed, the interface shear and transverse stresses are equal to those applied on the RVE (Equation 2-34)

$$\begin{cases} \sigma_i = \sigma_{yy} \\ \tau_{external} = \tau_{xy} \end{cases} \tag{2-34}$$

Having obtained all the stress components, which can exist on the overlap, we can proceed to propose a failure criterion by correlating all feasible stresses. Multiplying σ_i and τ_i (Figure 2-9) by the largest area of the tablet gives the corresponding forces exerted on the organic interface at overlap. It is worth to mention that these forces are perpendicular with respect to each other because the transverse and the shear stresses are orthogonal. Therefore, the resultant force can be written as

$$(\tau_i A_{Tablet})^2 + (\sigma_i A_{Tablet})^2 = F^2 = c \tag{2-35}$$

where A_{tablet} is the cross sectional area of the tablet (obtained by multiplying the length of tablet by its width). At failure, the capacity of the organic spring in carrying load, which is a constant material property of organic interface, is reached. Hence, the right side of Equation 2-35 will be constant (c) when the interface fails. Dividing Equation 2-35 by A_{tablet} gives

$$\tau_i^2 + \sigma_i^2 = \frac{F^2}{A^2_{\ Tablet}} = \frac{c}{A^2_{\ Tablet}} = c' \tag{2-36}$$

Taking into consideration that τ_i is the summation of two shear stress components, τ_i can be rewritten as

$$\tau_i = \tau_{external} + \tau_{axial} \tag{2-37}$$

By substituting Equations 2- 33, 2-34 and 2-37 into Equation 2-36, we obtain

$$\sigma_{yy}{}^2 + \left(\frac{\sigma_{xx}(t_t + t_i) - \sigma_i{}^y t_t}{l_o} + \tau_{xy} \right)^2 = c \tag{2-38}$$

where c is a constant that should be determined from experimental data. It should be noticed that the above failure criterion is applicable to any state of multiaxial tensile stresses on nacre.

In Equation 2-38, the external shear stress is assumed positive if follows the same direction of the axial stress. The question that may arise is whether the failure criterion is still valid for negative external shear stress. The answer to this question can be found by referring to the RVE (Figure 2-1). In the RVE, there are two overlap regions which might fail: overlap 1 above the axis of symmetry and overlap 2 below it. In Figure 2-12, possible orientations for the external shear stress are shown. Complete arrows depict the shear stress induced on the interface from the axial tensile stress, while half arrows represent the external (macroscale) shear stresses transferred to interface.

When a positive shear stress is applied on the composite (Figure 2-12a), overlap 2 will be the critical region and will fail sooner than the other because both shear stress components in this overlap are in the same direction and accelerate failure. On the contrary, overlap 1 will first undergo failure when a negative shear stress is applied on the composite.

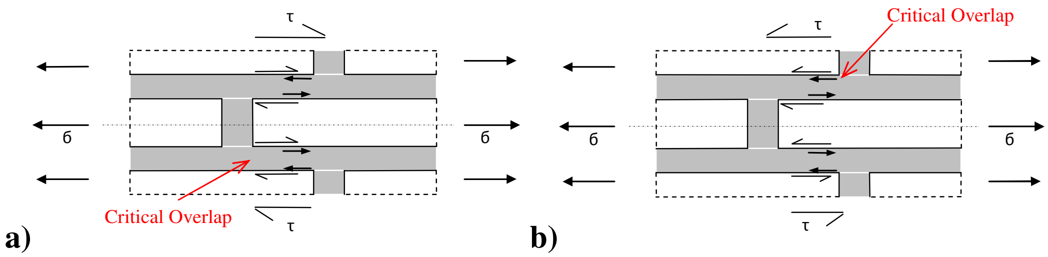

Figure 2-12: Possible failure conditions of overlaps in RVE: a) positive external shear stress b) negative external shear stress

Regardless of the sign of the external shear stress, the two shear stress components in one of the overlaps will be in the same direction. So, there is always a critical overlap susceptible to failure. Hence, the proposed failure criterion can predict the failure of the nacreous composite when the external shear stress is either positive or negative. Equation 2-38, can be modified to exclude the sign effect of the external shear stress by using the absolute value.

$$\sigma_{yy}^{\ 2} + \left(\frac{\sigma_{xx}(t_t + t_i) - \sigma_i^{\ y} t_t}{l_o} + \left| \tau_{xy} \right| \right)^2 = c \tag{2-39}$$

The experimental data from the tensile test across the tablet on nacre is chosen to calculate the value of c in Equation 2-39. When nacre is pulled normal to the plane of tablets, the strength of nacre is almost the same as that of the organic material at the interface. In fact, the stress is carried through the adjacent layers of the mineral tablets and organic material in order that the same stress is observed at each layer. Hence, the strength of nacre, when loaded across the tablet, is independent of the tablet geometry, as it can be seen in Equation 2-39. In this case, $\sigma_{xx} = \tau_{xy} = 0$ and the term $\sigma_i^{\ y}$ is also zero because there is no axial stress capable of stretching the junction. Therefore, Equation 2-39 will be simplified as

$$\sigma_{yy}^{\ 2} = c \tag{2-40}$$

Replacing the yield strength of interface results in $c = (\sigma_i^{\ y})^2$. Now, Equation 2-39 can be modified as

$$\sigma_{yy}^{\ 2} + \left(\frac{\sigma_{xx}(t_t + t_i) - \sigma_i^{\ y} t_t}{l_o} + \left| \tau_{xy} \right| \right)^2 = (\sigma_i^{\ y})^2 \tag{2-41}$$

The failure criterion proposed in Equation 2-41, can be used to predict the failure of nacre under combined multiaxial loading conditions. In this criterion, the axial strength of nacre depends on the geometry of the tablet and the interface as well as the corresponding material properties, while the strength across the tablet is constant for a given interface.

The uniaxial tensile strengths of nacre in the plane of the tablet are tabulated in Table 2-1 for the case of sheet and columnar nacre. Experimental data of the seashells of Pinctada [43] and Trochus Niloticus [39] were selected for the sheet and columnar nacre, respectively. The strength predicted by the failure criterion is found to be less than the experimental data. The failure criterion was derived based on several simplifying assumptions whereas in the actual nacre, more complicated features, e.g., tablet waviness and nanoasperities, exist that boost the tensile strength of the structure. However, the result of analytical formulation could approximately validate the experimental data.

Table 2-1: Comparison of in-plane strength of sheet and columnar nacre

Type of nacre	L_t (μm)	t_t (μm)	t_i (μm)	l_o / L_t	In-plane strength (MPa)	
					Experiment	Analysis
Sheet	4	0.5	0.028	0.5	130	118
Columnar	10	0.82	0.02	0.2	85	83

This chapter focused on the microstructure of nacre to modify the available relations for in-plane young modulus of nacre. The effects of overlap and junction were considered to develop a model representing the actual microstructure of nacre. In addition, a failure criterion was proposed to predict the nacre failure under multiaxial state of tensile stresses. In the following chapter, the macroscale structure of a typical gastropod seashell is modeled utilizing the results obtained in this chapter. By using this model, we will investigate how a mollusk animal uses the two-layer shell as an armor system to protect itself against natural predators.

Chapter III Macroscale Modeling

As discussed in the previous sections, seashells use a two-layer ceramic based armor system for protection against sharks or impact loads due to falling of rocks. In nature, seashells are found in a variety of shapes, sizes and material structures. Most of the bivalve and gastropod seashell species are composed of two layers, with nacre as the inner layer and calcite as the outer layer [29]. Abalone and pearl oyster are two examples that contain these two categories of materials (Figure 3-1).

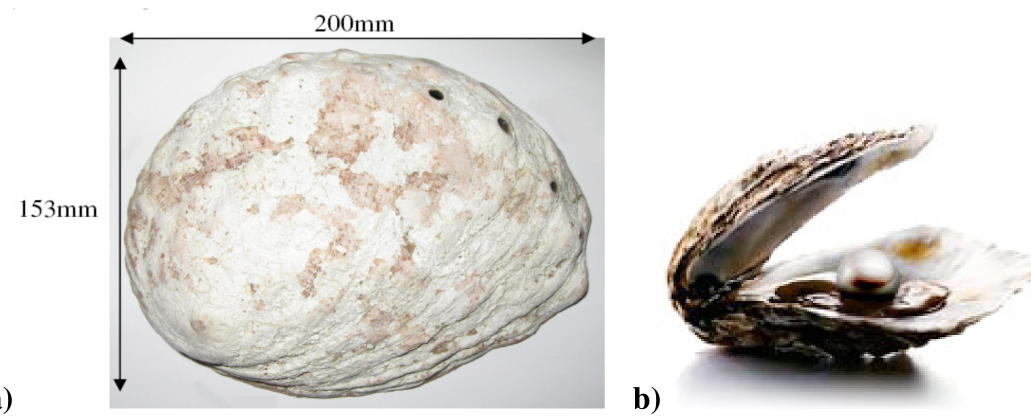

a)

Figure 3-1: a) Red abalone b) Pearl oyster

To investigate how seashells use two different materials as a protective layer, a simplified model of red abalone is developed in this chapter. Two layers of distinct materials are considered. To represent the load from the tooth of a shark, a spherical load distribution is applied on the shell. Finally, two failure criteria are used to formulate the general failure mode of the whole structure.

3.1 Axisymmetric Two-Dimensional Model

To develop a model of a seashell from the gastropod or bivalve class, we considered the red abalone because first its nacre as well as its microstructure are relatively well understood. In addition, its macrostructure makes it relatively easy to model as a spherical cap.

Red abalone's structure (Figure 3-2) is similar to an ellipsoidal cap. It is found in a wide variety of sizes from smaller in younger shells to larger in older ones. The thickness of the shell varies at different locations. Generally, the thickest part is observed in the middle and the thinnest part at the edges. The range of different geometrical parameters of a typical adult red abalone shell is shown in table 3-1.

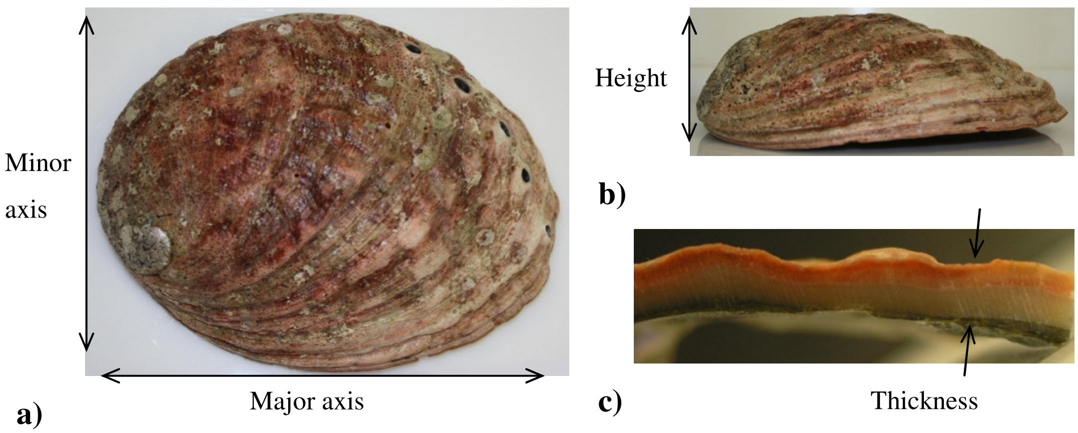

Figure 3-2: Geometrical parameters of red abalone seashell

Table 3-1: Measurement of various dimensions of an adult red abalone shell

	Minor axis (cm)	**Major axis (cm)**	**Height (cm)**	**Thickness (mm)**
Measurements	16 ± 2	20 ± 2	7 ± 1	6 ± 3

The hierarchical structure of red abalone is presented by its geometry at the macroscale and materials governed at the microscale. In order to investigate the multiscale structural and material characteristics of the seashell, a relatively simple model is created in ANSYS (ANSYS, Inc., Canonsburg, PA) based on the geometry of red abalone. Since the modeling and analysis of the actual structure with finite element packages is difficult, some assumptions are required. It is assumed that (i) the shell has a uniform thickness; (ii) its shape can be approximated with a spherical cap and (iii) the shell is in full contact with the support (all points of the edge contribute to the load transfer to the ground).

Based on these assumptions, an axisymmetric two-layer model of the seashell is developed in ANSYS (Figure 3-3). In this model, the outer and inner layers represent calcite and nacre, with corresponding material properties, respectively.

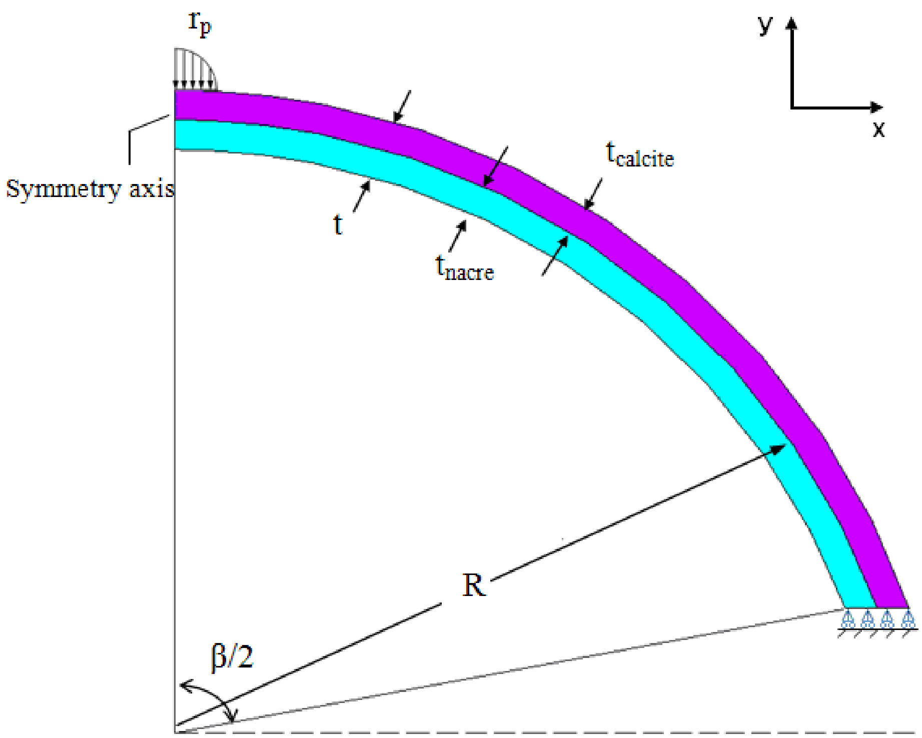

Figure 3-3: Structural parameters of seashell

In Figure 3-3, R and t are the average radius of curvature and thickness of the shell, respectively. β is the opening angle of the spherical cap. In order to model a sharp contact load, e.g., from a predator's tooth, a spherical distribution of pressure consistent with contact stresses was imposed on a small region at the apex of the shell [70, 71]. The corresponding applied pressure is written:

$$P(r) = \frac{3}{2} P_m \left(1 - \left(\frac{r}{r_p} \right)^2 \right)^{1/2} \tag{3-1}$$

where r_p is the radius of contact load and r is the distance from an arbitrary point of the distributed load area to the symmetry axis of the shell. P_m is the average pressure within the contact region defined as

$$P_m = \frac{P_{Load}}{\pi r_p^{\ 2}} \tag{3-2}$$

where P_{Load} is the total amount of the load carried by the contact pressure load. The rim of the shell was assumed to be simply supported. A symmetric boundary condition was also imposed on the symmetric axis of the shell, which also satisfies the necessary conditions to restrict the horizontal rigid body motion.

ANSYS Plane42 axisymmetric elements were used to discretize the layers with given material properties. The mesh at the apex of the shell was refined in order to capture the high gradients of the contact stress field. To reduce the computational cost, coarse meshing was used far from the contact area and close to the rim, where the effect of the load is less important (Figure 3-4).

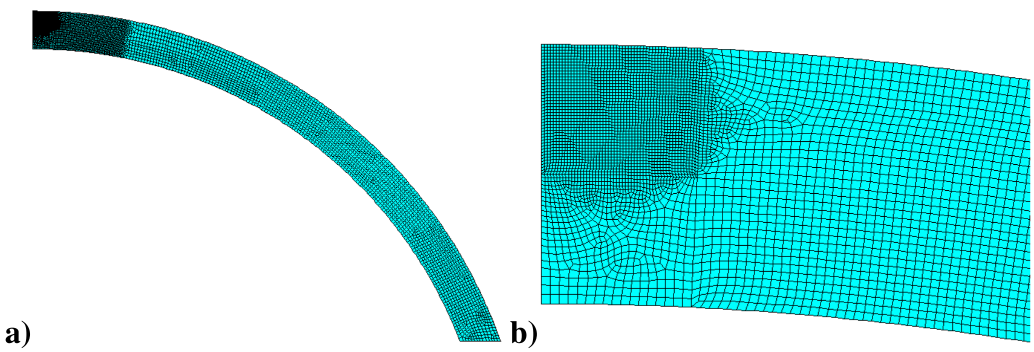

Figure 3-4: Shell mesh a) whole cross section b) refined mesh near the contact load

3.1.1 Calcite as outer layer

The outer layer of the shell is made of calcite, ($CaCO_3$), an isotopic material which is hard enough to protect the soft tissue of animal against natural dangers. However, it shows brittle behavior at failure. To model calcite a Young's modulus of 100 GPa and Poisson's ratio of 0.3 were assumed [66]. Principal stress in calcite was used to predict its brittle failure. It was assumed that failure occurred when the largest principal stress in any point of the calcite layer exceeds its maximum strength, which is 100 MPa [66].

3.1.2 Nacre as inner layer

Nacre forms the inner layer of the seashell. The unique microstructure of nacre with relevant toughening mechanisms gives nacre a very high toughness and is capable of undergoing relatively large inelastic deformations. Here nacre was modeled as a transversely isotropic material, with the local out-of plane direction corresponding to the shell's radial direction. The in-plane elastic modulus derived in Chapter 2 was used as the corresponding elastic modulus in the plane of the tablets. Out-of-plane elastic modulus was formulated by assuming that the transverse stress is uniform within the tablet and interface layers [50]. Therefore, using the Reuss composite model, we obtain

$$\frac{t_i + t_i}{E_{Out-of-plane}} = \frac{t_t}{E_t} + \frac{t_i}{E_i} \tag{3-3}$$

where t_t, t_i, E_t and E_i are thickness and elastic modulus of the tablet and interface respectively and $E_{Out-of-plane}$ is the out-of-plane elastic modulus of nacre. Poisson's ratio was assumed to be 0.2 in all directions [48], which is a usual value for a ceramic material [72].

In-plane shear modulus was formulated by assuming isotropic property in the plane of the tablet.

$$G_{In-plane} = \frac{E_{In-plane}}{2(1+\upsilon)} \tag{3-4}$$

where υ is the corresponding Poisson's ratio. To determine the out-of-plane shear modulus, the same assumption as the in-plane elastic modulus was made. Using Reuss model, out-of-plane shear modulus was obtained as

$$\frac{t_i + t_i}{G_{Out-of-plane}} = \frac{t_t}{G_t} + \frac{t_i}{G_i} \tag{3-5}$$

where G_t and G_i are the shear moduli of tablet and interface respectively.

The failure of nacre was modeled using the failure criterion derived in Chapter 2 for tensile multi-axial state of stresses. Compressive stresses in nacreous layer were considered for few typical cases to figure out whether nacre fails in tension or compression and it was found that nacre likely fails in tension rather than in compression because its compressive strength is relatively much higher than the tensile one [47]. Therefore, the effect of the compressive stresses was not considered further

3.2 Appropriate Coordinate System

When the shell is subjected to a point load, multiaxial stresses will be induced. In the case of a spherical shell, the most appropriate coordinate system, which can demonstrate all related stresses and geometrical parameters, is the spherical coordinate system.

In Figure 3-5, the notation used in spherical coordinate system is illustrated. The stress perpendicular to the surface of the shell is called normal stress and is shown by σ_{zz}. Meridional stress ($\sigma_{\varphi\varphi}$) and circumferential stress ($\sigma_{\theta\theta}$) are those along meridian and equator of the spherical shell, respectively. $\tau_{\varphi z}$ is the corresponding shear stress in $\varphi - z$ plan. It is worth noting that shear stresses in the equatorial directions are zero due to the symmetry of the problem ($\tau_{\theta z} = \tau_{\theta\varphi} = 0$).

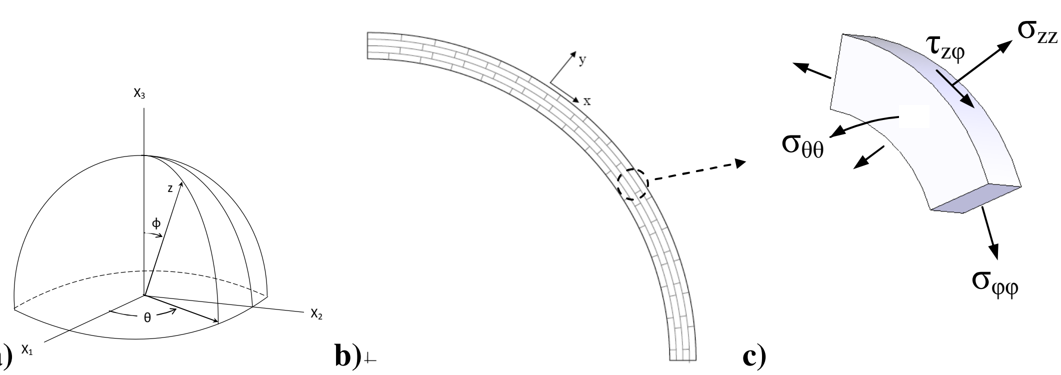

a) b) c)

Figure 3-5: Spherical coordinate system: a) spherical coordinates; b) local coordinate system compatible with tablet orientation; c) different stresses on a three-dimensional element of the shell

The failure criterion derived in Chapter 2 was obtained in the global Cartesian coordinate system whereas the stresses from the finite element analysis are in the spherical system. In order to be consistent with the spherical coordinate system, the failure criterion is modified to include all available stresses. This can be done by choosing a local coordinate system similar to the one used for RVE as described in the previous chapter (Figure 3-5). Therefore, the failure criterion (Equation 2-41) is modified as

$$\begin{aligned} &\sigma_{zz}{}^{2}+\left(\frac{\sigma_{\theta\theta}(t_t+t_i)-\sigma_i{}^{y}t_t}{l_o}\right)^2+ \\ &\left(\frac{\sigma_{\varphi\varphi}(t_t+t_i)-\sigma_i{}^{y}t_t}{l_o}+\left|\tau_{\varphi z}\right|\right)^2=(\sigma_i{}^{y})^2 \end{aligned} \tag{3-6}$$

3.3 Failure Criterion for the Shell

The two-layer structure with the constituent materials is solved for a given load to compute the stresses within the structure. A load of 1kN is applied on the apex of shell through the spherical contact area. The finite element model returns the corresponding stresses in the calcite and nacre layers. Using the failure criteria for nacre and calcite, a "Failure Ratio" (λ) was computed for the nacreous and calcite layers. From this failure ratio, and using the linearity of the stress analysis, the maximum load that the shell can carry was determined. λ measures the stress at a point of the shell with respect to the shell strength. For each of two layers, a particular relation of λ is defined as:

$$\lambda_{Calcite}=\max\begin{cases}\dfrac{\max\{\sigma_1,\sigma_2,\sigma_3\}}{S_{ut_{Calcite}}}: & \text{assuming}\ \sigma_1>0\\ \dfrac{\min\{\sigma_1,\sigma_2,\sigma_3\}}{-S_{uc_{Calcite}}}: & \text{assuming}\ \sigma_3<0\end{cases} \tag{3-7}$$

where σ_1, σ_2 and σ_3 are the principal stress components and $S_{ut_{Calcite}}$ and $S_{uc_{Calcite}}$ are the ultimate tensile and compressive stresses of calcite, respectively. In Equation 3-7, the effects of the tensile and compressive stresses were considered to predict the real cause of calcite rupture.

$$\lambda_{Nacre} = \frac{\text{Nacre Equivalent Stress}}{\text{Transvere Strength of Nacre}} = \frac{\sigma_{Nacre-eq}}{S_{Nacre-transverse}} \tag{3-8}$$

where $\sigma_{Nacre-eq}$ is the equivalent stress for nacre using the previously derived failure criterion (Equation 2-41)

$$\sigma_{Nacre-eq} = \sqrt{\sigma_{zz}{}^2 + \left(\frac{\sigma_{\theta\theta}(t_t + t_i) - \sigma_i{}^y t_t}{l_o}\right)^2 + \left(\frac{\sigma_{\varphi\varphi}(t_t + t_i) - \sigma_i{}^y t_t}{l_o} + \left|\tau_{\varphi z}\right|\right)^2} \tag{3-9}$$

For all points of the shell, the failure ratio is calculated according to the material of the constituent layer. When λ is less than unity, the point for which λ is calculated is safe. $\lambda = 1$ means that failure occurs at the considered point.

For a given load on the shell, stresses and consequently failure ratio for all points of the structure are computed. The point with the highest λ is prone to failure ahead of other points. Thus, the location of the highest value of λ determines the critical point

$$\lambda_F = \max(\lambda_{Nacre}\ and\ \lambda_{Calcite}) \tag{3-10}$$

Value of λ_F depends on the amount of the load exerted on the shell. Since it is of interest to calculate the maximum load that the structure can support, the amount of the load for which λ_F is equal to unity is desired. Using linear elasticity theory, the maximum load is calculated as

$$P_{\max} = \frac{P_{Initial}}{\lambda_F} \tag{3-11}$$

where $P_{\max}$ is the maximum load that the shell can carry and $P_{Initial}$ is the pre-sumed load (1 kN here) by which the problem is solved and λ_F is computed ac-cordingly. Using this approach, the ultimate load that the shell can carry is ob-tained and the location of the critical point is also recognized.

Failure can occur at different locations on the shell depending on the values of the geometrical parameters, i.e., thickness of the shell, average radius of curvature of the shell and the ratio between the thicknesses of calcite to the total thickness [26]. The thickness of the shell and the amount of calcite in the structure are the key parameters in the locating the failure. In sections to follow, the different fail-ure modes of the shell structure are explained.

3.3.1 Failure due to contact stresses

In this case, Hertzian contact stresses control the failure. The configuration near the contact point is similar to a sphere in contact with a half space. According to the contact stress field, the maximum principle stress occurs on the surface of the shell, right at the edge of the contact area, and is believed to be responsible for the formation of Hertzian conical crack [71]. Figure 3-6a shows the failure mode due to contact stress at the outer layer. Typically, this type of failure was prominent for the shells with the thick calcite layer.

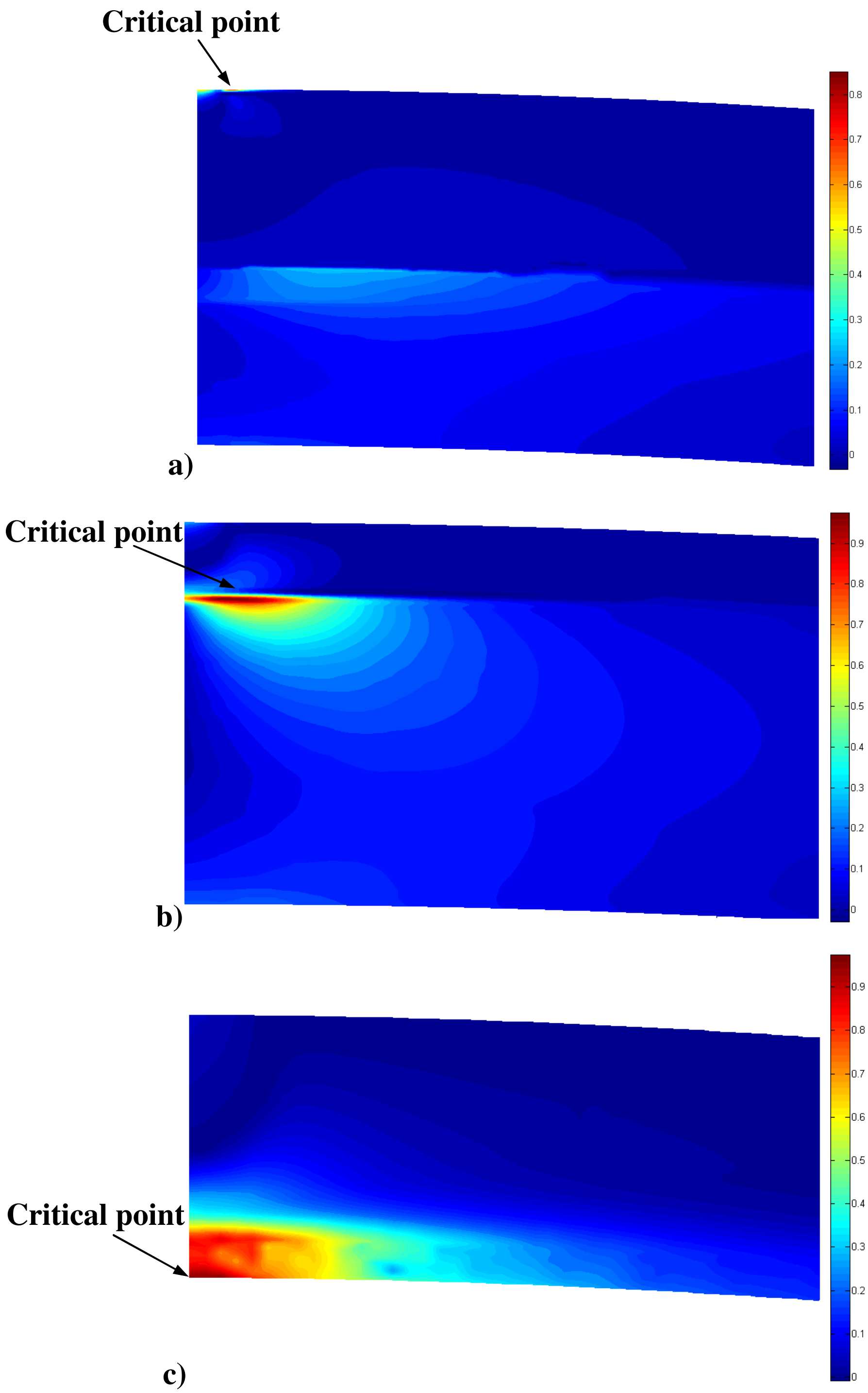

Figure 3-6: Contour plots of failure ratio (λ) to determine the failure point: a) failure at the calcite layer due to contact stresses; b) failure initiated at the interface of two layers in nacreous side; c) failure at the inner surface of the shell due to flexural stresses

3.3.2 Failure at the interface of two layers in nacreous side

For thick shells with a thinner calcite layer, the failure occurs at the interface calcite / nacre. In this case, the effect of contact stress field is observed at the interface of the two layers. Since nacre has lower strength than calcite, it is prone to failure although the stresses on the points of two sides of the interface do not differ remarkably. Therefore, failure is observed at the interface of two layers in nacreous side (Figure 3-6b). At the failure point, the equivalent stress defined by the failure criterion for nacre, which is a combination of multiaxial stresses, is the highest throughout the nacreous layer.

3.3.3 Failure due to flexural stress

In addition to contact stresses, which are generated from the indentation, flexural stress can contribute to the failure. Flexural stress is generated by bending of the shell. For the case of a spherical shell under a concentrated load applied at its apex, maximum tensile and compressive flexural stresses occur at the middle axis of the shell (φ=0) on the inner and outer surface of the shell, respectively. Flexural failure competes with contact failure. For a thick shell, flexural stresses are smaller than contact stress while for thin shells flexural stresses are prominent. The shell therefore will fail in bending dominated mode instead of contact failure (Figure 3-6c).

The finite element model was used to identify the influence of the shell thickness (t) and the ratio of thickness of calcite to shell thickness (α_c) on the mode of failure of the shell and obtain the transition between the failure modes. In Figure 3-7, the transition map of the three failure modes is shown for the radius of curvature of the shell equal to 0.1 m.

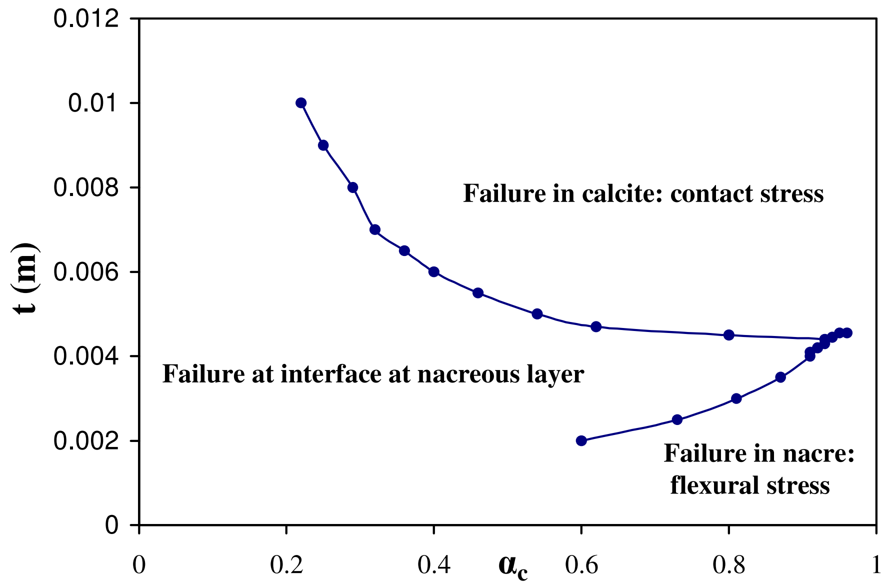

Figure 3-7: Transition map of the three failure modes

As mentioned, the failure modes are important in the analysis of a two-layer shell because they determine the region where the failure crack initiates. They are determined by the geometrical parameters and the material properties of the shell. From a design point of view, recognition of the critical point of a structure is crucial because the design can be improved to fortify the region prone to failure.

In the next chapter, a parametric study will be performed on the macroscale parameters to capture the transition between the possible modes of failure and perceive their role on the maximum load carrying capacity of the structure. In addition, an optimization strategy will be developed to identify the optimum values of multiscale parameters for which the strongest structure is obtained.

Chapter IV Multiscale Optimization

In the present chapter, an optimization study on the seashell structure and materials is accomplished to investigate how seashell geometry and material are optimized to resist penetration. The finite element model of a red abalone seashell, as was presented in the preceding chapter, is used as the basic model for structural optimization. In the first part, attention is mainly focused on the macroscale parameters, i.e., radius of curvature of the shell, shell thickness, opening angle and calcite/shell thickness ratio, to obtain the optimum structure by which the shell can support the highest load at its apex. In the second part, the effect of nacre microstructure is also included into the optimization formulation to investigate the effect of nacre microscale parameters on the overall strength of the seashell.

4.1 Optimization Scope

Optimization techniques were used to determine the microstructure and macroscale geometry of the seashell, which can withstand the highest amount of load. The optimization aims at coupling the effect of the microstructure of nacre to the macroscale structural features of the actual seashell. The microscale aspects are governed by the analytical solution of the mechanical properties and the multiaxial failure criterion of the nacreous layer. The seashell finite element model, described in Chapter 3, is used for the structural analysis.

4.1.1 Optimization variables

As described above, the finite element model of the shell consists of four geometrical parameters at the macroscale, namely, the average radius of curvature of the shell (R), shell thickness (t), opening angle (β) and the ratio of thickness of calcite to shell thickness (α_c) (Figure 4-1a). The whole geometry of the shell can be expressed in terms of these four parameters. In addition to the four geometrical parameters, the radius of contact load is another variable that expresses the load distribution. Since the load carrying capacity of the shell depends on the load contact area, both the thickness and the radius of curvature were normalized with respect to the contact radius:

$$R^* = \frac{R}{r_p},\ t^* = \frac{t}{r_p} \tag{4-1}$$

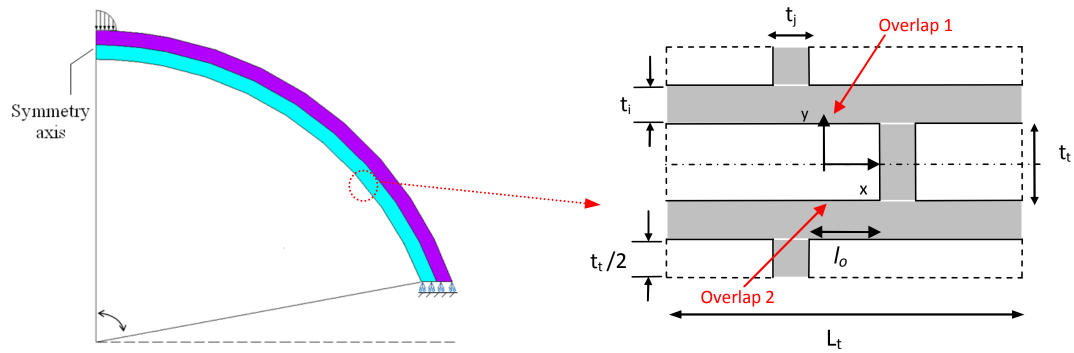

a) **b)**

Figure 4-1: Optimization variables: a) at the macroscale; b) at the microscale

Consequently, the results of the modeling and optimizations can be scaled for any structure with similar geometry and loading conditions. To be consistent in normalizing the parameters with respect to the contact radius, the load that the shell can support was also normalized. As a result of examining the effect of the contact radius on the load, as will be discussed later in another section, it was observed that the total load that the shell can support is proportional to the square of contact radius. If for a prescribed contact radius (r_{p_o}) the shell with a given t^* and R^* withstands the maximum load of $P_{\max_o}$, then the load that another shell with the same t^* and R^* can carry under any given contact radius can be predicted as

$$P_{\max} = P_{\max_o}\left(\frac{r_p}{r_{p_o}}\right)^2 \tag{4-2}$$

In addition to the structural variables at macroscale, the mechanical properties of nacre are also expressed in terms of the material properties and dimensions of the mineral tablets and organic interface (Figure 4-1b). Except for the material properties of nacre constituents, which are almost constant for different seashells, the microstructural geometry and arrangement of the tablets have a strong influence on the mechanical properties of nacre. To investigate the effect of microscale structural features on the overall seashell strength, the tablet aspect ratio, the overlap size and the thickness of interface (Figure 4-1b) are considered as variables. Three dimensionless parameters are defined as follows:

$$t_t^* = \frac{t_t}{L_t},\ t_i^* = \frac{t_i}{L_t} = \frac{t_j}{L_t},\ l_o^* = \frac{l_o}{L_t} \tag{4-3}$$

where t_t, t_i, t_j, L_t and l_o represent the thickness of tablet, interface and junction, and the length of tablet and overlap, respectively. It is assumed that the junction has the same thickness as the interface. The analytical formulations derived for the modulus is re-written here as a function of these dimensionless variables:

$$E_{In-plane} = \frac{\mathrm{t}_t^*}{\mathrm{t}_t^* + \mathrm{t}_i^*} \frac{1}{\left(\frac{1}{E_t} + \frac{1}{E_i}\frac{N'}{1+N'}\mathrm{t}_t^*\right)} \tag{4-4}$$

where

$$N' = (\alpha' t_t^* t_i^* \frac{E_i}{G_i})\left[\frac{1+\cosh(\alpha' l_o^*)}{\sinh(\alpha' l_o^*)} + \frac{1+\cosh(\alpha'(1-l_o^*))}{\sinh(\alpha'(1-l_o^*))}\right]$$

and

$$\alpha' = \sqrt{\frac{4G_i}{t_t^* t_i^* E_t}}$$

Likewise, the general form of the failure criterion (Equation 2-41) can also be expressed in terms of the dimensionless variables as

$$\sigma_{yy}^{\ 2} + \left(\frac{\sigma_{xx}(t_t^* + t_i^*) - \sigma_i^y t_t^*}{l_o^*} + \left|\tau_{xy}\right|\right)^2 = (\sigma_i^y)^2 \tag{4-5}$$

4.1.2 Optimization formulation

The goal of the optimization study is to maximize the load that the shell can carry at its apex (P_{Load}). As mentioned in the preceding section, in this multiscale optimization study six variables control the performance of the seashell model where three of them represent the macroscale geometry of the shell and the other three belong to microstructure of nacre. The optimization problem can be described as:

$$\text{maximize} \quad P_{Load} = f(R^*, t^*, \alpha_c, t_t^*, t_i^*, l_o^*) \tag{4-6}$$

$$\text{subject to} \quad \begin{cases} 10 < R^* < 800, \\ 1 < t^* < 40, \\ 0.5 < \alpha_c < 0.95 \\ 0.02 < t_t^* < 2, \\ 0.001 < t_i^* < 0.5, \\ 0.1 < l_o^* < 0.5 \end{cases} \tag{4-7}$$

The variables were constrained within upper and lower boundaries, specified by the available information about the geometry and the material models of the sea-shell as well as the type of the loading. The definition of the constraints allow for ignoring unfeasible regions of the design space where the variables assume non practical values, such as negative values for the geometric parameters. Therefore, boundaries are defined to limit the range by which each parameter can vary. It follows that the box constraints are assumed in the optimization study to let variables change in a valid range, which are not so far from the actual properties of sea-shells.

4.1.3 Optimization strategy

The optimization algorithm was developed in MATLAB (The MathWorks, Inc., Natick, MA) whereas the structural analysis was accomplished in ANSYS. The link between MATLAB and ANSYS is shown in Figure 4-2. MATLAB is capable of running ANSYS automatically with a "dos" command. Therefore, MATLAB handles the whole procedure by feeding ANSYS with a text file that contains the information to run ANSYS for the seashell structure analysis. For each iteration, the results from ANSYS are exported into MATLAB, read and optimized by the algorithm.

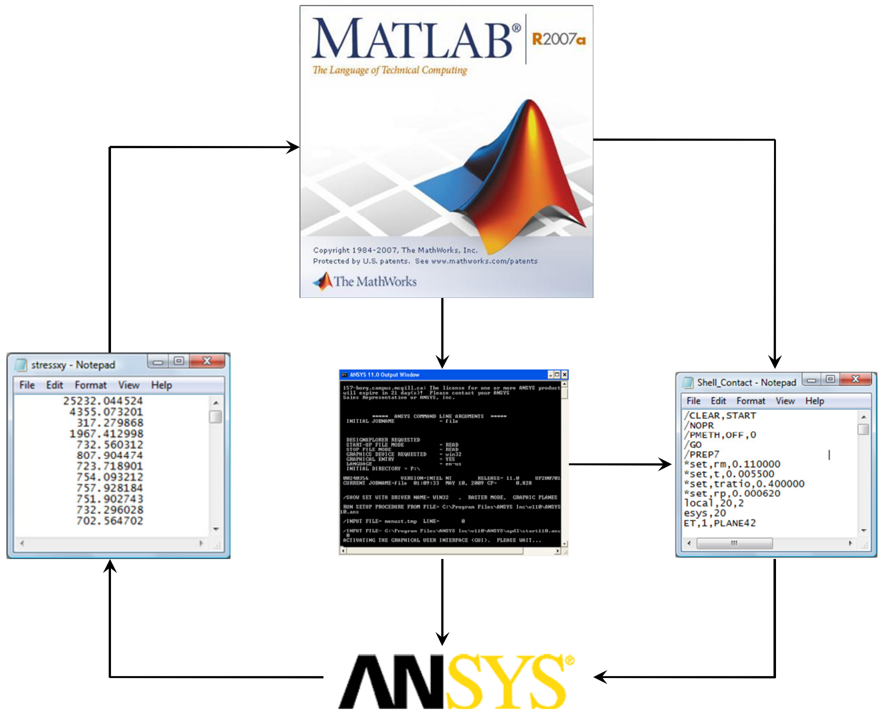

Figure 4-2: Connection between MATLAB and ANSYS

4.2 Optimization Techniques

In this section, a brief review of the optimization methods [73] will be presented to explain the appropriate methods for executing the optimization strategy mentioned in the preceding sections. Selecting an appropriate optimization technique is one of the most important steps to solve an optimization problem. The number of objective functions and their formulation (analytical or numerical solution) as well as the number and types of constraints (equality and inequality constraints) and design variable (discrete or continuous variables) are key features for the selection of an appropriate optimization method.

The number of the objective functions in an optimization problem classifies the methods into two main categories: when an optimization problem modeling a physical system involves only one objective function, the task of finding the optimum solution is called *single-objective optimization* and if the optimization problem involves more than one objective function, it is called *multi-objective* *optimization* [74]. Since just one objective function (the load that the shell can support) exists in our optimization problem, the single-objective optimization techniques are considered here to choose the suitable optimization method.

To this date, several single-objective optimization algorithms have been proposed whose performance totally depends on the type of the problem generality. Although various approaches have been recommended to classify the available optimization algorithms for structural applications, the comparison of optimization techniques based on the objective function gradient has been more intensively used [75]. Techniques that require the gradient of objective function for moving toward the optimum solution are called gradient-based methods whereas direct search methods just need the objective function value for finding the optimum result without any gradient calculation. Gradient-based methods are not suggested to be used if the closed form solution of the objective function is not available or there is a high number of design variables. However, the fast convergence rate of gradient–based methods is a significant advantage compared to direct search methods. Since a finite element model including up to six design variables is used in this work, gradient-based techniques were disregarded to opt for direct search techniques. Direct search methods have the benefit of avoiding the calculation of the gradient information of the objective function that is remarkably advantageous where the number of design variable is high or a mathematical closed form solution of the objective function is not available or a discontinuity in the objective function is observed through the design space, albeit they converge slower than the gradient-based methods.

The initial attempts to find the optimum solution of a problem by using the objective function value can be made without any specific algorithm. The Enumeration Search is one method that calculates the value of the objective function for any combination of design variables before selecting the best one [76]. Enumeration Search methods are well suited to visualize the objective function trends on a map of the design space as a function the design variables. Constraints can also be plotted to restrict the design space. While capable to explore the entire design

space and to ensure the selection of the optimum point, these methods often require a huge computational cost which limits their application to problems with a low number of variables.
Except the Enumeration Search, all other direct search methods use an algorithm to approach the optimum solution. Generally, direct search methods can be categorized into two parts: Probabilistic and Deterministic methods.

Probabilistic methods: these methods use a random function to generate the initial points and start to move toward the global optimum by improving those points in different iterations [77]. Dependant on the random solution generation, the results achieved by these methods are not reproducible. Genetic Algorithm (GA) [78], Simulated Annealing (SA) [79] are the most well known and frequently-used probabilistic algorithms.

Deterministic methods: in contrast to the probabilistic methods, deterministic techniques, which follow a unique path for any given initial point, look for the optimum by restarting the search at different points of the design space [80]. Simplex method is the most renowned example of deterministic methods.

Since there are up to six variables in our optimization problem, Nelder-Mead simplex method (NM) was opted as the appropriate optimization algorithm [81]. Probabilistic methods were ignored because of the large computational cost that is often involved during the search. Therefore, NM algorithm and its characteristics are described in details in the following section.

4.2.1 Nelder-Mead simplex algorithm

As a non-gradient based technique, the simplex method was first proposed by Nelder and Mead in 1965 [81]. In an n-dimensional space, NM method employs a simplex of (n+1) points for finding its way toward the optimum solution. Once the initial simplex, which is for instance a triangle in two-dimensional space, is generated, the objective function is computed for all the simplex vertices. Then, NM method tries to improve the current simplex by replacing the worst point with a more favorable point. The worst point of the simplex is the one with the lowest function value in a maximization problem or vice versa, the one with the highest function value in a minimization problem.

$$P^* = \overline{P} + \psi(\overline{P} - P_w) \tag{4-8}$$

where P^* is the new point, which replaces the worst point. $\overline{P}$ and P_w are the centroid and the worst point of the current simplex, respectively. ψ is the parameter that controls the operation by which the simplex is improved.

During the search, a number of operations, e.g., reflection, expansion, contraction, are applied to the worse point of the simplex to find another point that has a superior objective function. By examining the required operations, the simplex is updated with a more favored one and this process is repeated until the size of the simplex becomes less than a user-defined value, where the algorithm is stopped and the optimum solution is obtained.

In the first step to improve the simplex, the worst point is reflected with respect to the centroid of the simplex, which is known as a *reflection* operation ($0 < \psi$). If the new point has a better function value than the worst point but less than the other simplex points, the worst point is replaced with the new reflected point. If the reflected point has a more favorable function value than all the simplex vertices, the move is expanded along the line connecting the worst point and the reflected one, through the *expansion* operation ($1 < \psi$). If the expanded point has an improved objective function value, then it replaces the worst point, otherwise, the reflected point is chosen. When neither the reflection nor the expansion operations lead to an improvement in the current simplex, a *contraction* ($-1 < \psi < 0$) is applied to the worst point which will be moved within the simplex. If applying these three operations does not bring about any improvement in the current simplex, the simplex is shrunk toward the best point of the simplex.

Selecting the suitable value of ψ for each enhancing operation is the challenging part of using the simplex method because they can affect the convergence rate. Employing the NM technique for optimizing a variety of mathematical and practical objective functions yielded that the best performance is generally achieved by setting the ψ equal to 1, 2 and -1 for the reflection, expansion and contraction operations, respectively [81-83]. However, in some cases other values of ψ may lead to a better performance, which totally depends on the type of the problem. The convergence rate of NM method is controlled by the value of the reflection, expansion and contraction parameters. The number of design variables also influences the rate of convergence, where the NM method is found to be practical for the problems with less than 10 design variables [84].

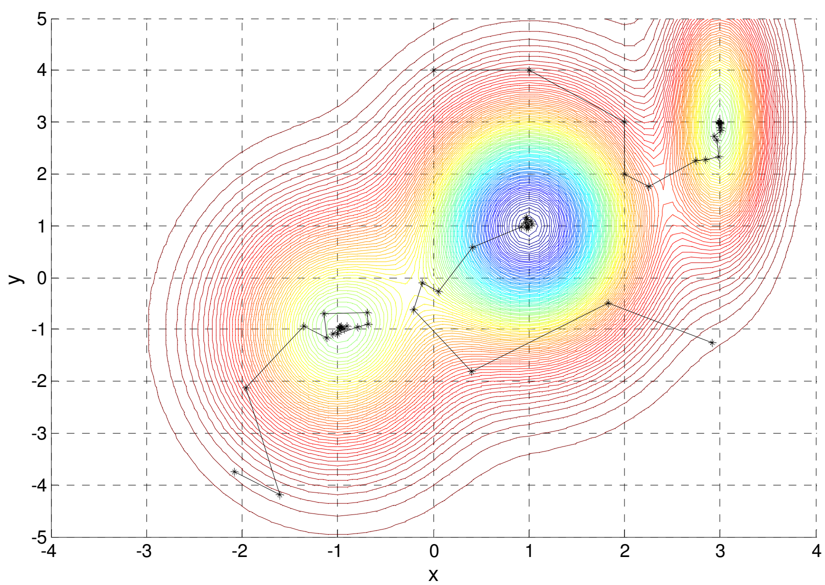

Figure 4-3: Dependency of convergence of Nelder-Mead simplex method on the initial simplex

The performance of NM algorithm always depends on the assumed initial simplex. NM simplex method is executed by calculating the value of the objective function for a set of points to decide its way toward the optimum solution. So, when approaching to the optimum point, it just evaluates the function value of some points close to the simplex and does not examine the other region of design space. Therefore, it is always possible for the simplex to be trapped into a local solution. Figure 4-3, illustrates the convergence of NM method for a mathematical function for three different initial simplexes. The function contains a global minimum centered at (1, 1) and two local minima at (-1, -1) and (3, 3). The centroid of the simplex at each step is illustrated in Figure 4-3 to track the path that the algorithm follows when approaching the minimum solution. It is observed that for various initial guesses, the algorithm converges to the different optima.

4.2.2 Coupled Nelder-Mead algorithm and random generator

As mentioned, NM method does not guarantee to find the global optimum and it is feasible to being trapped into a local solutions. Since we are interested in locating the global optimum for the seashell structure and material, NM method should be examined for different initial guesses to ensure that the best solution is achieved. This is done by developing an algorithm to generate different initial simplexes [85-87]. A random generator is used to define the vertices of the simplex totally in a random fashion. Therefore, by starting from different initial simplexes within the design space, the NM algorithm explores different paths to find the best solution. Increasing the number of starting points raises the chance of converging to the global result, although the convergence of NM has been proved only for one and two dimensional problems [83, 84, 88]. The hybrid NM technique was used in our work to explore different paths within the design space toward the optimum solution.

4.3 Optimization with respect to t^* and α_c

Normalized shell thickness (t^*) and calcite to shell thickness ratio (α_c) are found to have the most significant influence on the strength of the shell. For this reason, the first investigation focuses on the effect that these variables have on the load carrying capacity of the shell. All the other variables were fixed. The opening angle was set to 140^o, similar to that of an actual shell of red abalone. A dimensionless radius of curvature (R^*) of 200 was assumed to simulate a sharp load on the shell. The material properties of the constituent layers were also set according to the experimental data from the actual shell of red abalone, as explained in detail in chapter 3.

Three different approaches are here applied to find the optimum structure. One approach is the hybrid NM described in the preceding section, the others fall within the class of enumeration methods.

4.3.1 Modified NM simplex method

The modified NM with random generator technique was applied to trace the optimum solution. It was run for 100 random initial simplexes and it converged to different points located on a curved line. The results are shown in Figure 4-4, where the red solid circles point out the converged results for each of initial guesses.

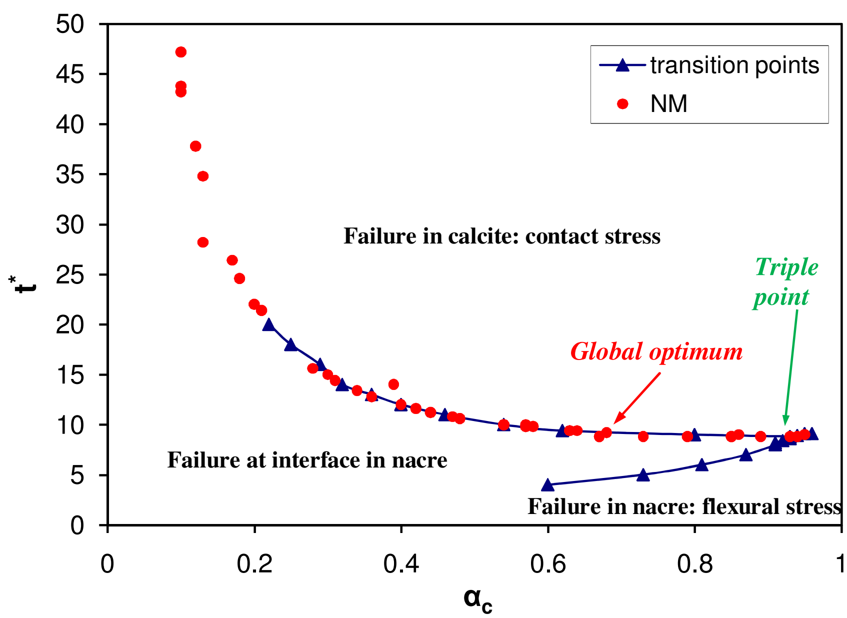

Figure 4-4: NM method and enumeration search constraining the transition between different modes of failure

4.3.2 Enumeration search: transition between failure modes

Concurrently to approach 1 described in section 4.3.1, a parametric study was performed to find the boundaries between the three failure modes explained in chapter 3. To tackle this challenge, α_c was manually altered for any given value of t^* to locate the transition point. Three different lines were obtained, which represent the boundaries between three regions. The blue solid triangles in Figure 4-4 demonstrate the transition between each of two feasible failure modes. The triple point in Figure 4-4 represents the point where the three modes of failure coincide in the structure and the three failure transition branches intersect. The transition line between the failure in calcite and the flexural failure in nacre, which is located on the right side of the triple point, is found to be small compared to the other lines.

4.3.3 Enumeration search: exploration of the entire design space

In order to visualize the effect that each of the two described parameters, i.e., α_c and t^*, can have on the load carrying capacity of the shell, any possible combinations of the two variables were tried to explore the whole design space. Although the exploration is somehow cumbersome, it illustrates the sensitivity of the maximum load to the changes of the design variables. Therefore, the result of other methods can be validated by direct comparison of the results with the visualized design space. In Figure 4-5, the load resistance is demonstrated within the design space for a limited range of each parameter.

4.3.4 Comparison of the three techniques

Three different approaches were employed to track the optimum structure, which can support the highest load, assuming that just two independent variables exist. The results are obtained for $R^* = 200$. In this case, NM method converged to a global optimum point with t^* and α_c equal to 8.8 and 0.65, respectively. As it was expected, NM stopped at different points rather than being converged into the global optimum. As it is viewed in Figure 4-5, no local maximum exists in the design space. In fact, a "ridge-like" surface appears in the design space whose

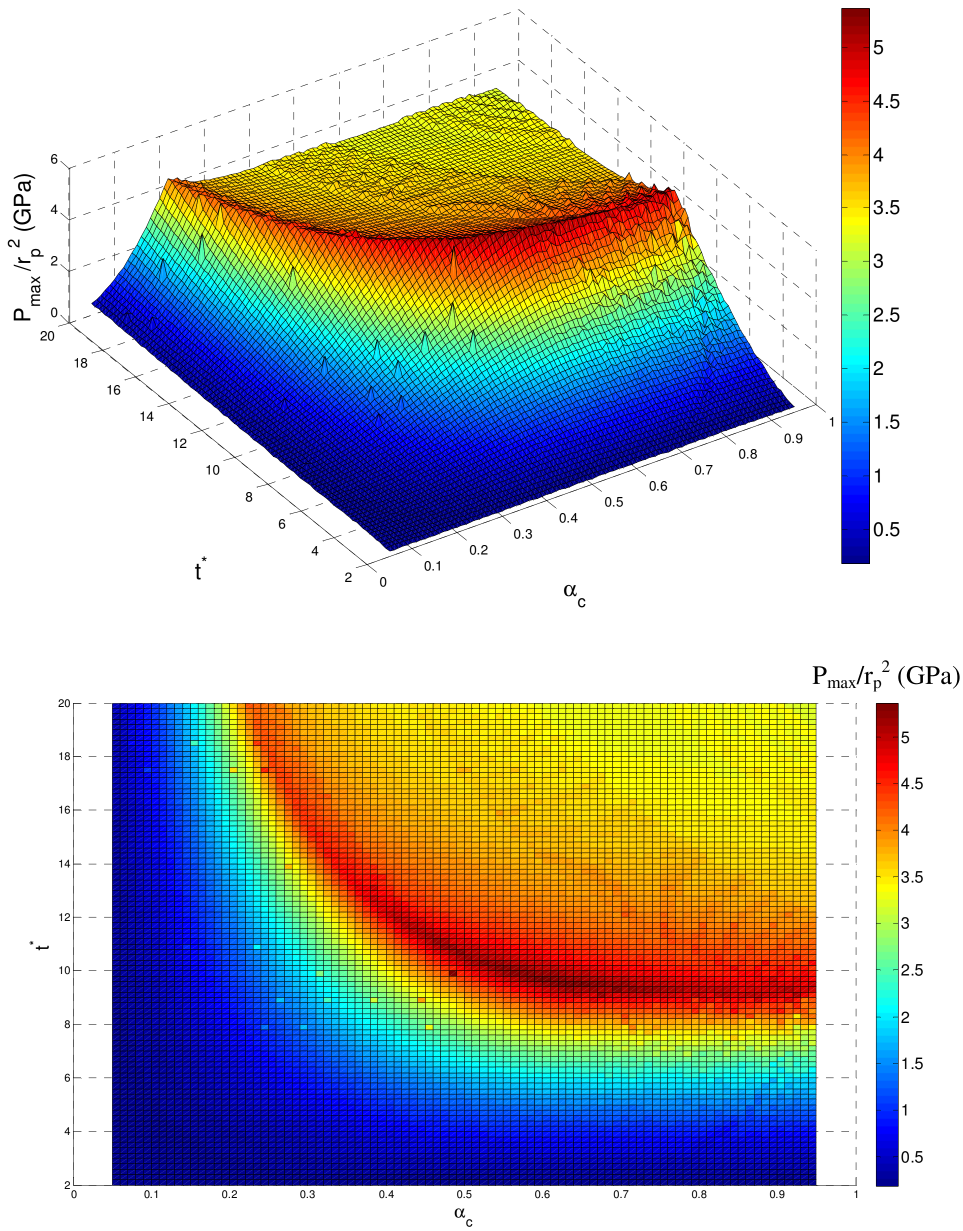

Figure 4-5: Visual map of design space for two parameters

summit is the global maximum. Although no local optimum exists within the design space, the NM method converged into different locations on the ridge of the mountain. This phenomenon occurs when a simplex climbs up the mountain until it reaches the ridge and cannot move along the ridge anymore. Once the simplex is at the top of the mountain, it tries to replace the worst point with a more favored one, which can be only found along the ridge. If the ridge is sharp, as in our case, the chance of moving on the ridge towards the peak is very low. Therefore, when the simplex reaches a point on the ridge, it cannot find a better point using available operations and the algorithm starts to shrink and after some iteration, terminates. Thus, starting the NM method from different initial points increases the chance of finding the points of the ridge as well as the global optimum.

A closer examination of the optimization results and failure modes revealed that the ridge of the mountain in the design space map actually matches the transition between failure in calcite layer and failure in nacreous layer.. This concept was first explained by Weaver and Ashby [89], where they investigated the failure of a column under various loadings. They considered three failure modes for rupture of a column, i.e., global bucking, local buckling and plastic collapse and found that the optimum design corresponded to the case where three modes of failure coincided. The same scenario was discovered in our results. When two modes of failure happen together in two different layers, both layers collaborate in withstanding the load and the failure damage is distributed evenly in two layers rather than being concentrated in a specific location. In this case, the structure utilizes more materials to resist the load, which leads to a higher strength of the structure.

The exploration of the design space presented in Figure 4-5 verifies the idea that the maximum load carrying capacity of the shell structure happens when two modes of failure coincide in the calcite and nacreous layers, either the nacreous failure occurs at the interface of the two layers or at the inner surface of the shell due to the flexural stress.

4.4 Optimization with respect to All Macroscale Variables

In this section, the effect of the radius of curvature of the shell is also considered in the optimization study. The NM simplex method was employed to optimize the two-layer shell structure with respect to the all three macroscale parameters. As mentioned in section 4.1.1, the macroscale variables were normalized with respect to the contact load radius. At this stage of the optimization strategy, we first aim at verifying the procedure that was followed for normalizing the macroscale variables. Thus, dimensional macroscale variables, namely, the radius of curvature of the shell (R), the thickness of the shell (t) and the ratio of thicknesses of calcite and the shell (α_c), were considered here and the optimum solution was obtained for different radii of contact load to prove the relationship between the contact load radius and the optimum shell structure. In other words, we aim at showing the trend by which the optimum shell structure varies due to a change in the contact load radius as an independent variable. For instance, if the radius of the contact load is doubled how the optimum shell changes. As a result of finding the dependency of the optimum shell structure on the contact load radius, the method that was used for normalizing the geometrical variables of the shell will be verified.

For a given contact radius, the simplex technique was run for 80 randomly generated initial simplexes and the optimum values for dimensional macroscale variables were obtained. Then, the results were compared to investigate the relationship between the optimum macroscale variables and the contact radius. Table 4-1 shows the results of optimization for five contact radii.

Table 4-1: Results of shell geometry optimization with respect to three macroscale variables

Fixed variable	**Optimum variables**			
r_p (mm)	**R (cm)**	**t (mm)**	**α_c**	**P_{max} (N)**
0.25	6.93	2.7	0.42	365.8
0.4	11.2	4.1	0.58	927.2
0.5	16.36	5.2	0.47	1295
0.75	27.68	8.5	0.47	3361
1.00	31.41	11.1	0.55	5859

As it can be observed in Table 4-1, by changing the contact radius, the optimum values for the shell thickness and radius of curvature vary linearly, but the maximum load that the shell can carry changes proportionally with the square of contact radius (Figure 4-6). The optimal α_c is found to be around 0.5, which means that half of the thickness of the shell is occupied with calcite.

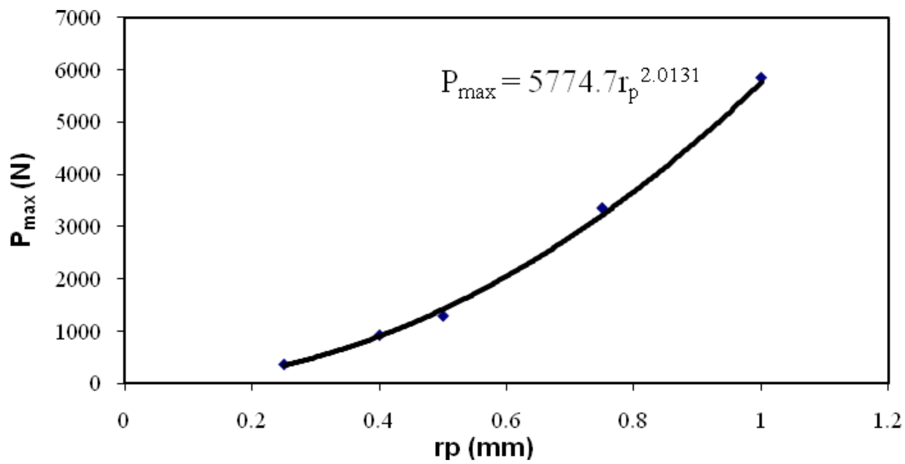

Figure 4-6: Load versus contact radius for the optimum structure

Hence, the normalization of the geometrical variables of the shell with respect to the contact radius is precise where for a given contact radius, the optimum structure can be predicted. Dimensionless structural variables for the optimum structure are tabulated in Table 4-2.

Table 4-2: Optimal dimensionless macroscale variables

R^*	t^*	α_c	$P_{max}/(r_p)^2$ (GPa)
300.17	10.7	0.49	5.8528

It is remarkable to mention that the maximum contact pressure (P_m) that the shell can withstand is the same for all optimum structures. By increasing the contact area, the amount of the load transferred via the indenter increases linearly however the optimum shell structure changes in such a manner that the contact pressure remains constant.

The results in this section were achieved by fixing the material properties of the constituent layers to those of an actual shell of red abalone. The opening angle of the shell was also set similar to the abalone shell. Based on the optimization results, α_c is found very close to the actual shell, where nacre and calcite comprise half of the shell thickness. The optimum shell structure depends on the contact area and the structure of the shell. An actual shell of red abalone is about 5 mm thick and has a radius of curvature of about 12 cm. Using the information of the dimensionless optimum seashell, it was found that the red abalone shell is best designed to face "threats" of radius of 0.45 mm.

4.5 Multiscale Optimization

The final step of this study, involves the development of a multiscale optimization that can capture the influence of nacre microstructure on the strength of the shell. Therefore, the geometrical variables of the shell, which are presented at the macroscale, are considered together with the nacre microstructure variables with the aim of finding the best shell geometry and microstructure. As a result, six variables were present in this stage. Three of them existed at macroscale, namely, ratio of radius curvature of the shell to contact radius (R^*), ratio of shell thickness to contact radius (t^*), ratio of calcite layer thickness to shell thickness (α_c), and three other represented microscale variables, i.e., ratio of tablet thickness to tablet length (t_t^*), ratio of interface thickness to tablet length (t_i^*) and ratio of overlap length to tablet length (l_o^*).

NM simplex method was employed and started from 100 randomly initialized simplexes. As expected, the algorithm converged to various points within the design space because of complicated shape of the objective function. Six best results, which exhibit the highest strength of the shell, were selected and shown in Table 4-3. As seen in Table 4-3, the results do not converge to a certain point however all parameters fall into a small range compared to the boundaries assigned for each variable as mentioned in Equation 4-7. According to the results, the optimum shell might be selected from a narrow range of geometric and material variables rather than a unique selection, as it is found in nature where seashells of the same type exist in various sizes. By looking at the results of the microscale variables, it is observed that the optimum tablet and interface dimensions reached the lower boundaries. It occurred due to the fact that by making the tablet and interface thinner, the modulus and strength of nacre increases leading to better nacreous material properties. On the other hand, these dimensions cannot decrease further because of fabrication constraints and also failure of the tablet, which happens due to high stress transfer within the tablets. This phenomenon is also observed in nature where tablet aspect ratio increases up to the point where tablets fracture rather than the organic interface failure. The variation in the size of the overlap is also in a good agreement with existing information about columnar and sheet nacre seashells. In addition, all achieved optimum results took place at the transition of two failure modes, i.e., Hertzian contact failure in calcite layer and failure in nacreous layer initiated at the interface of two layers. As a result, the shell optimizes its materials and geometry in such a fashion that it makes the most of its materials to resist against penetration.

Table 4-3: Results of multiscale optimization with six variables

	Shell Geometry			**Microstructure**			$\mathbf{P_{max}/(r_p)^2}$ **(GPa)**
	R^*	t^*	$\boldsymbol{\alpha_c}$	t_t^*	t_i^*	l_o^*	
Run #1	366	8.5	0.63	0.02	0.001	0.44	7.354
Run #2	333	8.5	0.62	0.02	0.001	0.34	7.298
Run #3	428	9.4	0.66	0.02	0.003	0.2	7.207
Run #4	407	11	0.78	0.02	0.003	0.36	6.143
Run #5	412	15.8	0.34	0.05	0.012	0.4	6.097
Run #6	391	17.2	0.37	0.07	0.038	0.44	5.934

Chapter V   Penetration tests on actual seashells

Experiments were performed on actual shell of red abalone to investigate the response to penetration. A sharp indenter was used to simulate the load from a natural predator, e.g., the tooth of a shark. The load was applied at the highest point of the shell. The goal of these experiments was to measure the resistance to penetration of the shell and to identify its modes of failure. In this chapter, the detail of the experiment setup and techniques utilized to calculate the strain will be explained and, finally, the results of experiments will be discussed.

5.1 Experiment Description

Three intact shells of red abalone were purchased from a shell shop (Specimen shells, Halifax NS) and kept in water to maintain hydration. For the experiments, the shells were laid on a custom made fixture (Figure 5-1a) in a mechanical loading machine (MTS Systems Corporation, Eden Prairie, MN). The shells were punctured at their apex via an indenter connected to the load cell of the mechanical loading machine. The software package supported by the MTS machine allows exporting information about the load, the crosshead displacement and the time during the test.

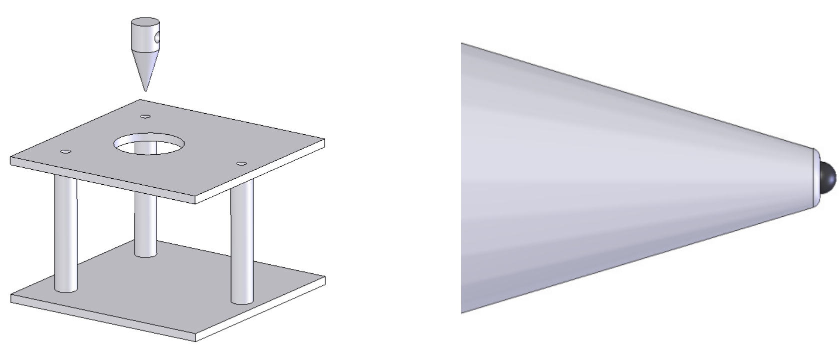

a) **b)**

Figure 5-1: a) schematic of the experiment setup; b) tungsten carbide ball embedded into the tip of the indenter

The inner surface of the shell underneath the indentation site was imaged through a hole in the base plate (Figure 5-1a) with two CCD cameras. VIC3D digital image correlation system (Correlated Solutions, Columbia, SC) was then utilized to determine the three dimensional deformation of the inner surface of the shell from the stereo imaging information from the two cameras. Digital image correlation computes the deformation of an area by comparing the image of the deformed shape with the reference image. For proper correlation, the desired surface must include random patterns with enough contrast. In this work, the surface inside the shell was covered with a very thin layer of white mat paint and black speckles were sprayed on the white background to generate a random pattern (Figure 5-2). By analyzing the information of acquired images, the three dimensional deformation and strains of the inner surface of the shell were determined at different instants during the experiment.

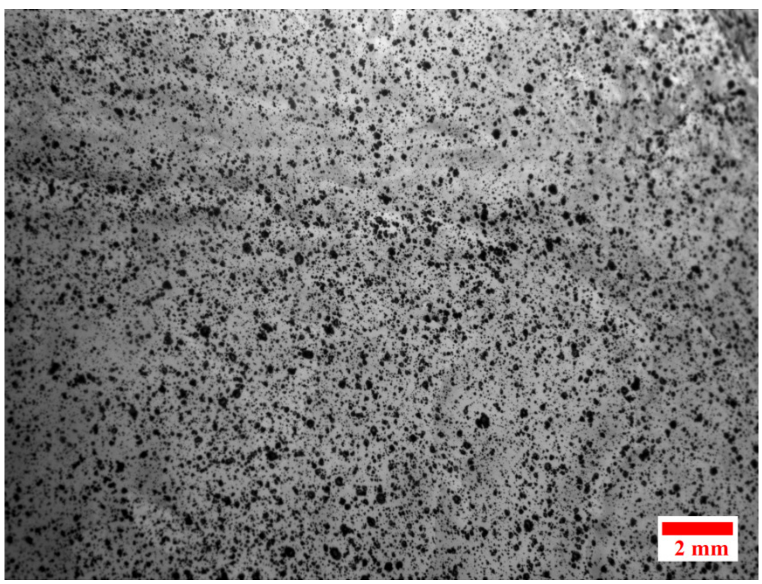

Figure 5-2: Random pattern created on the inner surface of the shell

An actual picture of the experimental setup is shown in figure 5-3. Flexible links carrying lights at their tips were employed to illuminate the area inside the shell. A tungsten carbide ball of 1mm in diameter was fixed on the tip of the indenter to transfer the load to the shell without deformation of the contact area (Figure 5-

1b). The size of the ball was chosen as small as possible to model a sharp contact area.

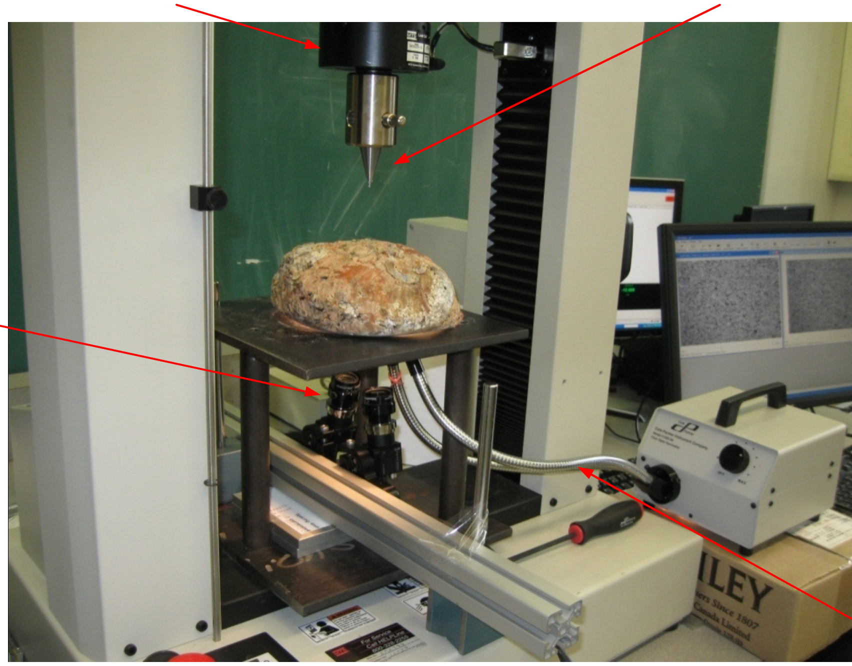

Figure 5-3: Experiment configuration

We tried to perform the experiments similar to the actual situation that seashell may confront in nature. For instance, no defect existed in the samples and no grinding or polishing was used to change the supporting points of the specimens. It is worth to mention that all samples were in contact with the underlying surface in three regions on different locations of the rim of the shell (Figure 5-4).

During the experiments, the crosshead of the loading stage was moved towards the shell with a rate of 0.5 mm/sec. VIC3D system was set up to save two photos of the desired surface per second. The information from MTS loading machine and VIC3D system was used to interpret the experiment and failure of the sea-shell.

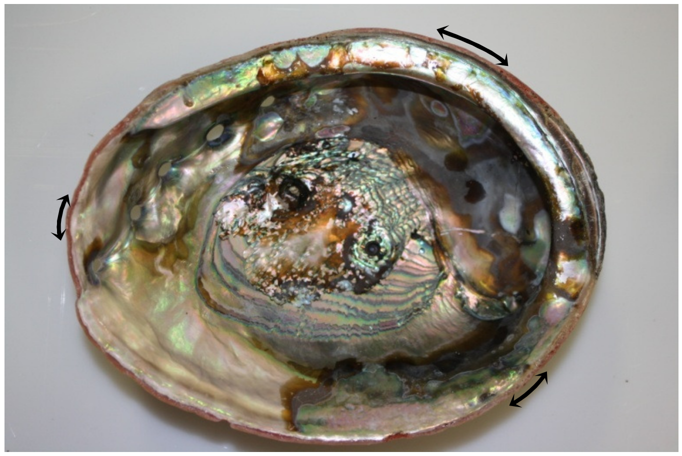

Figure 5-4: Supporting locations of red abalone shell on a flat surface

5.2 Experiment Results

Puncture experiments were performed on three intact samples of red abalone seashell. Load versus crosshead displacement curves of the three experiments are shown in Figure 5-5. A few points on the load-displacement curve were chosen to explain the failure behavior of the shell. From the experimental results, it was observed that the failure behavior of two samples in the first and the third experiments (Figure 5-5a,c) were identical, but the second sample failed with a noisy pattern in the load-displacement curve (Figure 5-5b). The noisy performance of the second specimen occurred due to the sliding and instability of the shell on the setup during the experiment and the rupture of some points of the rim of the shell. In fact, the data points between the points P and Q in Figure 5-5b took place during the instability of the shell on the setup; however, the slope of the curve before the point P and after the point Q were almost the same, which means that the shell is resisting against the penetration in a similar fashion.

The results of the first experiment (Figure 5-5a) were chosen to explain the way that the seashell failed under penetration. From origin to point A, the indenter penetrated into the calcite material. Calcite in the red abalone shell appeared to contain voids possibly generated by parasites. When the indenter was pressed

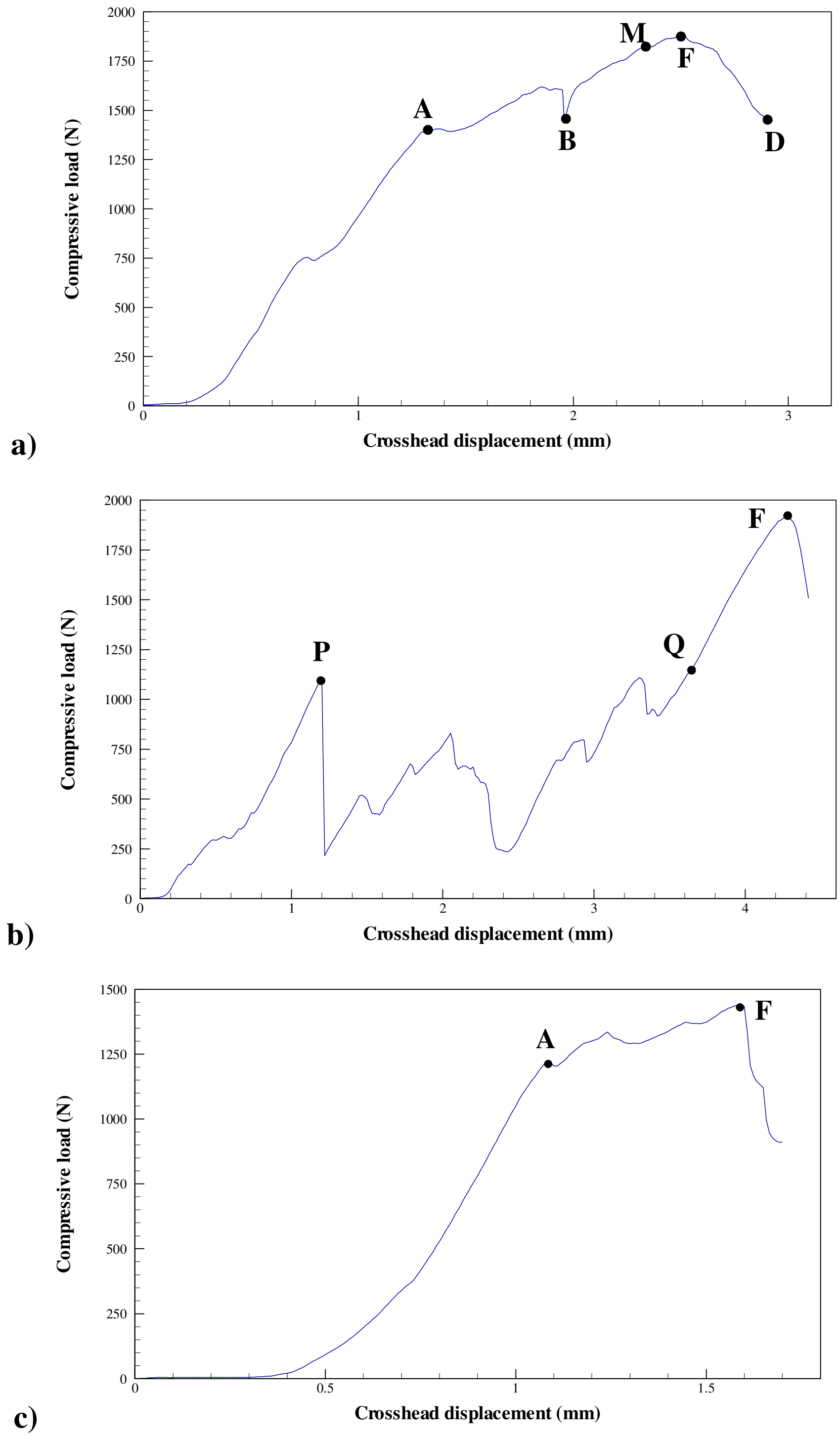

Figure 5-5: Load-crosshead displacement curve of the three experiments: a) Experiment 1; b) Experiment 2; c) Experiment 3. Point F in three graphs depicts the point where the flexural crack was initiated

against the calcite layer, it probably crushed the porous material underneath the contact region.

Although tiny cracks due to Hertzian contact stresses might be locally generated around the tip of the indenter, they were not important in rupturing the shell.

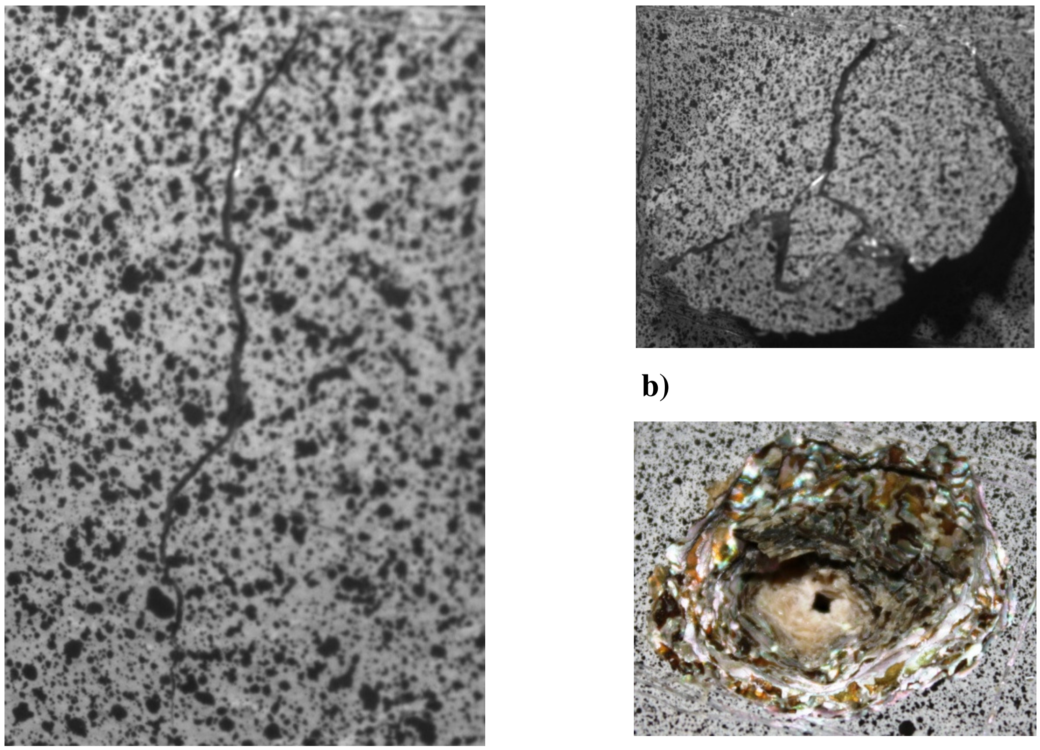

b)

c)

a)

Figure 5-6: Images of cracks at the inner surface of the shell: a) flexural crack; b) circular crack generated after the flexural and conical crack merged together; c) the conical hole formed inside the shell at the end of the experiment

By further continuation of the test, at point A, the shoulder of the indenter, which comprised the tungsten carbide ball, touched the surface of the calcite layer in addition to the ball and contributed in load transfer. In fact, both the ball and the tip of the indenter were carrying the load at this moment. After this point, the load had to be increased to penetrate into the calcite material. However, with the same amount of load the shell started to bend and the flexural stresses at the inner surface of the shell raised until point F, where a tiny crack was detected in nacre. It is worth to mention that a small piece of the rim of the shell broke at point B. The flexural crack is shown in Figure 5-6a for point D.

The load-displacement curve was not exported after point D because the crack was already detected inside the shell and the load-displacement information after this point did not help in comparing the results of the experiment and the numerical model. However, the test was continued after point D to investigate the failure behavior of the shell. The flexural crack at the inner surface of the shell opened until the point where the indenter pierced more deeply into the calcite material. At this instant, the influence of Hertzian contact stresses reached the interface of two layers and nacreous material felt the high Hetzian contact stresses. As a result, the conical crack propagated into the nacreous layer and moved toward the inner surface of the shell where it finally merged with the flexural crack and then, formed a circular crack on the surface (Figure 5-6b). As a result, a conical piece of the structure was cut out of the shell (Figure 5-6c) and loading was stopped.

After the experiment, a diamond saw was used to cut the seashell through the center of the conical hole. The two slices at the hole are shown in Figure 5-7. Several crack paths were observed in nacreous layer. The main crack established the conical hole with a large angle with respect to the axis perpendicular to the inner surface. As seen in Figure 5-7, some parts of nacre were pulled out of the composite and a crack was visible around those regions. This happened because when the conical crack was propagating, it was pressing the material down to the inner surface of the shell. In this case, layers of nacre were pushed down until a point where the material could not support high stress and cracks fractured those layers. In addition, at the interface of two layers, a crack due to delamination was detected.

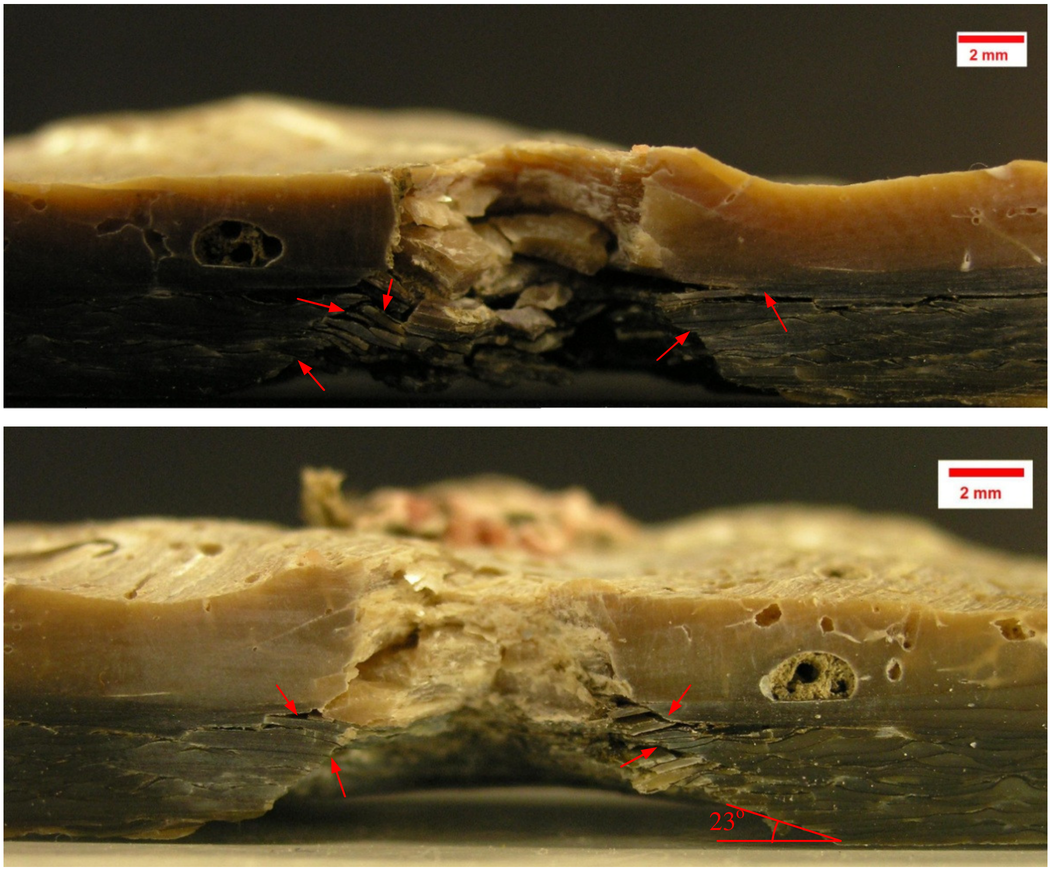

Figure 5-7: View of the cross section of the two pieces of the failed seashell after cutting with diamond saw. Arrows show the crack propagation directions

From the experimental results, it seems that when a crack is initiated in nacre, it tracks its path through the organic interface between the tablets. The crack tends to propagate along the high stress region but since the mineral tablet obstructs its path, the crack has to move along the weak interface. At some points, the crack is distributed into two branches, which decelerates the failure by spreading the crack along different directions and reducing the stress intensity at the tip of the crack.

In these experiments, the three modes of failure were observed. The calcite failed partially at the beginning of the test but it was not crucial because the porosity of the calcite hindered the crack propagation. Then, the flexural crack was detected in the inner surface of the shell. After this point, the conical crack initiated inside the structure propagated in the nacreous layer toward the inner surface of the shell where it merged with the flexural crack. Although there is not enough evidence to identify the exact moment when the conical crack initiated, the presence of conical crack in both layers was evident. Concurrent propagation of flexural and Hertzian conical cracks validates the optimization results, which show that the coincidence of failure modes make the shell stronger. In this case, the two modes of failure contributed in resisting against the penetration because the micro-structure arrangement of the seashell calcite and nacre was efficiently designed to postpone the shell rupture.

Using digital image correlation, the first principal strain was computed for the area on the inner surface of the shell and underneath the location of the indenter. Figure 5-8 depicts the principal strain for point M in Figure 5-5a before the point where flexural crack was detected. A high strain region is observed along a line where the flexural crack will be initiated afterward at point F. As a result, it was found that nacre undergoes a large plastic deformation where the first principal strain reaches 0.011, which is in good agreement with experimental data available in the literature for the maximum strain of nacre.

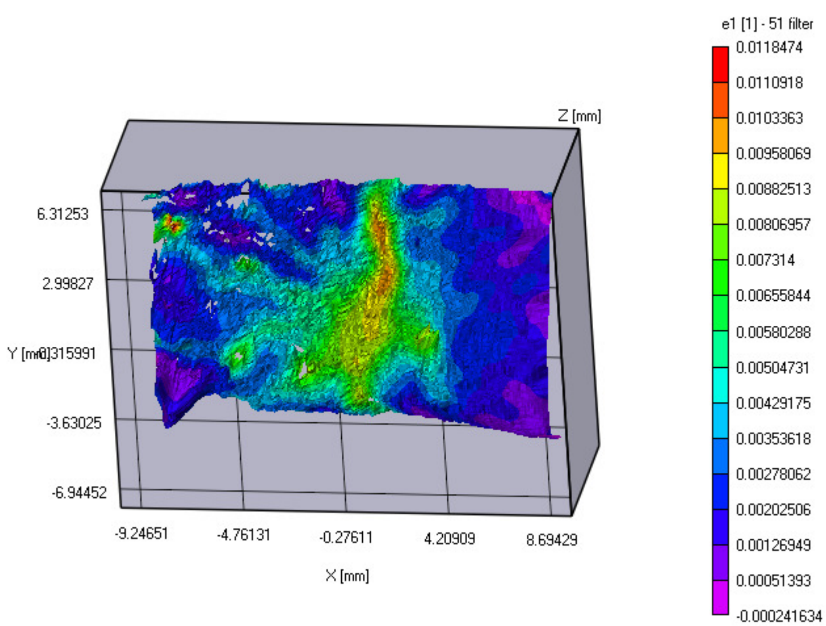

Figure 5-8: First principal strain for the area underneath the indenter on the inner surface of the shell before initiation of flexural crack

5.3 Comparison of Experimental and Modeling Results

Based on the geometrical parameters of the three samples of red abalone seashell, finite element models were developed to estimate the maximum load that the shell can resist before failure and to compare the computational results with the experimental data. From the experiments, the peak load of the load deflection curve, which corresponds to the initiation of the failure crack for all three samples, was chosen. The followings are the main assumptions of the finite element model which must be accounted for the results interpretation and discussion:

- The actual seashell structure is asymmetric; whereas in this work it is assumed to be a spherical cap.
- The thickness of the seashell changes through the shell. The thinnest part of the shell is usually found at the rim of the shell and the thickest part is located at the middle. In our model, a uniform shell thickness was considered through the whole structure.
- The porosity in calcite layer of red abalone seashell influences the behaviour of the shell. But in the model, it was assumed that the calcite is a solid material free of defects.

In order to model the structure of the shell, the radius of the contact area should be determined. The radius of the tungsten carbide ball was 0.5 mm but as it was observed during the experiments, the shoulder of the tip of the indenter also contributed in the load transfer, whose radius was 0.75 mm. Therefore, the contact radius in FEA modeling was assumed to be 0.75 mm to model the contact after the indenter touched the surface of the shell. Although the contact surface was not in a spherical profile when the indenter touched the shell because of the contribution of the indenter in transferring the load, the whole contact was assumed to occur through a sphere.

Table 5-1: Comparison of maximum load of modeling and experiments

	R (cm)	t (mm)	α_c	Load (N)	
				Modeling	Experiment
Experiment # 1	12	8	0.45	1729	1863
Experiment # 2	11	5.5	0.4	1227	1889
Experiment # 3	11	4	0.4	1097	1457

Table 5-1 compares the results obtained from the computational models and through the experiments. Considering all the assumptions made in the model, the agreement between the experiment and the model is remarkably good. The reason to the higher load of experiments can be explained by contribution of the indenter in the load transfer when it touches the surface of the shell in addition to the tungsten ball. In this case, higher load can be transferred to the shell due to an increase in the contact area. The largest discrepancy was in experiment 2, where the load reached a very high value but before this peak, instability was observed in the load-displacement curve due to the sliding and translation of the shell on the setup that could have affected the trend of the experiment.

The maximum load of the experiments corresponds to the point where the flexural crack was observed at the inner surface of the shell. The FEA modeling predicted that the failure initializes at the interface of the two layers of the shell in nacreous material. During the experiment, there was no possible method to track the deformation of the interface. However, both methods predicted that the failure takes place in nacreous layer.

From the experiments performed on the three shells of red abalone, it can be concluded that the actual seashell arranges its microstructure design to fully exploit its material properties and postpone failure, a result that was also obtained from the optimization study. The crack propagated through the thickness of the shell in three different failure modes. In addition, hydrated nacre undergoes large plastic deformation and absorbs high amount of energy prior to failure. Composed of typical ceramic material, the seashell can support up to 1900 N when loaded via a sharp indenter, which is surprisingly high compared to its size and structure.

Chapter VI Conclusions

6.1 Summary of Accomplishments

Multiscale modeling and optimization of seashell structure and material were reported in this thesis. Mollusk animals grow a hard ceramic shell, to protect themselves against natural predators. The structure of the shell is well designed over several length scales to make the most of the available materials and to maximize the protection of the mollusk animal. Utilizing different materials in the structure provides the seashell with a combination of various mechanical properties, which increases its strength and postpones its failure. Mostly composed of brittle ceramic materials found in nature, seashell wisely uses a mechanism governed at the microscale to produce nacre with remarkable toughness value.

In chapter one, the concept of biomimetics, its advantages and applications were explained. A thorough literature review of seashell and its constituents was also presented. Chapter two was devoted to the formulation of the mechanical properties of nacre. A representative volume element of nacre microstructure was proposed, by which the analyses were accomplished. As a result, the existing solution for in-plane elastic modulus of nacre was modified to include the effect of the overlap length and the junction between the tablets, which were overlooked before. From sheet to columnar nacre, the in-plane elastic modulus decreased about 10% when the effect of the junction between the tablets was excluded in the formulation. By taking the effect of the junction into consideration, the modulus increased about 18 GPa for sheet nacre and 23 GPa for columnar nacre. Furthermore, a multiaxial failure criterion for nacre was developed to predict its failure under combination of different states of stresses. In case of uniaxial tensile strength of nacre, the failure envelop could reproduce the experimental results with maximum error of 2% for columnar nacre and 9% for sheet nacre.

Chapter three described the multiscale modeling of the seashell. In this model, the geometry of the shell was controlled at macroscale with two layers, whereas the material properties of nacre were governed at microscale by employing the theoretical model derived in the preceding chapter. The shell was considered to be subjected to a concentrated contact load at its apex to model the attack from a predator. Two failure criteria were assumed for the layers to predict the failure of the seashell structure. Then, depending on the geometry of the shell, all possible modes of failure were introduced. Failure modes are important in predicting the manner by which the whole structure fractures.

Chapter four presented the optimization strategies that were used to obtain the strongest shell. It was observed that when two failure modes in nacre and calcite layers concur, the shell is capable of supporting higher amount of load. In this case, the shell structure exploits the materials capabilities at their full extent and distributes the stress into two different regions in order to avoid stress concentration. By performing optimization studies, we could predict the optimum shell configuration. If the microscale parameters, which control the material properties of nacreous layer, are fixed, we can design the shell geometry or loading condition to carry the highest load. From a designer point of view, if the loading condition is fixed as a constraint, the designer can relatively adapt the geometry of the shell to optimize its performance. On the contrary, if the shell geometry is kept constant, the loading condition can be optimized. For instance, in case of shell of red abalone, which comprises a fixed geometry, the optimum contact radius was found to be about 0.45 mm. In the next step toward optimization, the microscale parameters were also included in the optimization search to perform a multiscale optimization strategy. In this case, both the shell geometry and the microstructure of nacre were examined to obtain the optimal shell structure and material.

In chapter five, the results of experiments on the actual shell of red abalone were explained. Failure behavior of the seashell was investigated by performing penetration tests. During the experiments, it was observed that failure first took place in the calcite material due to the Hetzian contact stresses. But at a certain stage, the shell started to bend and flexural crack initiated in inner surface of the shell.

Then, the conical crack due to contact stresses and flexural crack propagated simultaneously until the point where a piece of the stsructure was cut off. Consequently, the concurrence of two modes of failure validated the optimization results, which predicted the coincidence of the failure modes. Therefore, the seashell was found to be optimally designed against penetration to employ most of its materials to support higher load prior to shell rupture.

6.2 Design Guidelines for Two-Layer Shell

From the results of optimization and experiments, some guidelines for design of a two-layer shell, which mimic the seashell structure for protection, can be summarized as follow:

- The combination of a hard outer layer with a tough and ductile inner layer leads to an ideal two-layer shell structure for protection purposes such as a helmet or aerospace applications. For our optimization we have determined that the thickness of the hard layer should be almost the same as the thickness of the tough layer (which is also the case in natural shells)
- A rather counterintuitive result is that thicker shells are not necessary stronger. For an optimum performance of the shell against the penetration, the thickness and the radius of the curvature of the shell should be 10.7 and 300.2 times greater than the radius of the contact load, respectively.
- The coincidence of failure modes makes the shell stronger against penetration and retards the failure of the whole structure. In this case, the shell employs strategically its materials to postpone the catastrophic failure.
- At the microstructure, a decrease in the thickness of tablet and interface with respect to tablet length in nacre microstructure makes the material stiffer and stronger; however, consideration of a lower bound for those dimensions is necessary to avoid the tablet rupture and meet the fabrication constraints.
- If the shell is supposed to be optimized against penetration with respect to both the geometry and the material, no unique solution exists, but the op-

timum solutions fall into a small region in the design space where all lead to the similar strength of the shell.

6.3 Future Work

As an extension to the work reported here, further studies can be performed in the areas of theoretical formulation, multiscale optimization and experiments.

- The proposed failure criterion can be modified with more accurate analysis. The effect of tablet waviness can also be included in the representative volume element for better representation of nacre microstructure.
- The failure criterion formulated in this thesis is valid for the tensile stresses along and across the tablets. The analysis can be extended to include the effect of the compressive stresses in order to present a more comprehensive form of the failure criterion.
- The shape of the shell was assumed here to be a spherical cap whereas in reality it is more similar to an ellipsoidal one. The shell model should be modified to be closer to the actual seashell shape.
- The variation in the shell thickness can be considered to better explore its performance.
- Behavior of the shell can be examined for other types of loadings such as an asymmetric penetration.
- Contact element is suggested to be used where the indenter touches the surface of the shell to obtain more accurate results.
- In the optimization part, several alternative strategies can be adopted to recognize the local optima. In addition, the problem could be formulated as a multi-objective optimization problem to retrieve optimum trade off solutions of the Pareto Front.
- Experiments can be done on other types of seashells to find out their performance.
- Alternative more refined techniques should be employed to identify the failure crack propagation along the shell thickness during the experiments.

Reference

1. Vincent, J.F.V., et al., *Biomimetics: its practice and theory.* Journal of the Royal Society Interface, 2006. **3**(9): p. 471-482.
2. Barthelat, F., *Biomimetics for next generation materials.* Philosophical Transactions of the Royal Society a-Mathematical Physical and Engineering Sciences, 2007. **365**(1861): p. 2907-2919.
3. Bhushan, B., *Biomimetics: lessons from nature-an overview.* Philosophical Transactions of the Royal Society A: Mathematical, Physical and Engineering Sciences, 2009. **367**(1893): p. 1445-1486.
4. Bhushan, B., Y.C. Jung, and K. Koch, *Micro-, nano- and hierarchical structures for superhydrophobicity, self-cleaning and low adhesion.* Philosophical Transactions of the Royal Society a-Mathematical Physical and Engineering Sciences, 2009. **367**(1894): p. 1631-1672.
5. Koch, K., B. Bhushan, and W. Barthlott, *Multifunctional surface structures of plants: An inspiration for biomimetics.* Progress in Materials Science, 2009. **54**(2): p. 137-178.
6. Nosonovsky, M. and B. Bhushan, *Hierarchical roughness optimization for biomimetic superhydrophobic surfaces.* Ultramicroscopy, 2007. **107**(10-11): p. 969-979.
7. Bechert, D.W., et al., *Fluid mechanics of biological surfaces and their technological application.* Naturwissenschaften, 2000. **87**(4): p. 157-171.
8. Bechert, D.W., et al., *Experiments on drag-reducing surfaces and their optimization with an adjustable geometry.* Journal of Fluid Mechanics, 1997. **338**: p. 59-87.
9. Abbott, S.J. and P.H. Gaskell, *Mass production of bio-inspired structured surfaces.* Proceedings of the Institution of Mechanical Engineers Part C-Journal of Mechanical Engineering Science, 2007. **221**(10): p. 1181-1191.
10. Reif, W.E., *Squamation and ecology of sharks.* 1985, Frankfurt am Main: Courier Forschungs-Institut Senckenberg.
11. Available from: http://www.ipaustralia.gov.au/media/pages/innovations/speedo.htm.
12. Bogue, R., *From bolometers to beetles: the development of thermal imaging sensors.* Sensor Review, 2007. **27**(4): p. 278-281.
13. Lenau, T., H.M. Cheong, and L. Shu, *Sensing in nature: using biomimetics for design of sensors.* Sensor Review, 2008. **28**(4): p. 311-316.
14. Mayer, G., *Rigid biological systems as models for synthetic composites.* Science, 2005. **310**(5751): p. 1144-1147.
15. Mattheck, C. and K. Bethge, *The structural optimization of trees.* Naturwissenschaften, 1998. **85**(1): p. 1-10.
16. Mattheck, C., *Teacher tree: The evolution of notch shape optimization from complex to simple.* Engineering Fracture Mechanics, 2006. **73**(12): p. 1732-1742.
17. Mattheck, C. and S. Burkhardt, *A new method of structural shape optimization based on biological growth.* International Journal of Fatigue, 1990. **12**(3): p. 185-190.

18. Mattheck, C. and S. Reuss, *The claw of the tiger-an assessment of its mechanical shape optimization.* Journal of Theoretical Biology, 1991. **150**(3): p. 323-328.
19. Abbott, R.T., et al., *Seashells of the world : a guide to the better-known species*. 1985, New York: Golden Press.
20. Kohn, A.J., *Encyclopedia of evolution: Mollusks*. 2002: Oxford Unversity Press.
21. Cortie, M.B., *Digital seashells.* Computers & Graphics, 1993. **17**(1): p. 79-84.
22. Illert, C., *Formulation and solution of the classical seashell problem .2. Tubular 3-dimensional seashell surfaces.* Nuovo Cimento Della Societa Italiana Di Fisica D-Condensed Matter Atomic Molecular and Chemical Physics Fluids Plasmas Biophysics, 1989. **11**(5): p. 761-780.
23. Illert, C., *Nipponites-mirabilis - a challenge to seashell theory.* Nuovo Cimento Della Societa Italiana Di Fisica D-Condensed Matter Atomic Molecular and Chemical Physics Fluids Plasmas Biophysics, 1990. **12**(10): p. 1405-1421.
24. Van der Helm, A., P. Ebell, and W.F. Bronsvoort, *Modelling mollusc shells with generalized cylinders.* Computers & Graphics, 1998. **22**(4): p. 505-513.
25. Zuschin, M. and R.J. Stanton, *Experimental measurement of shell strength and its taphonomic interpretation.* Palaios, 2001. **16**(2): p. 161-170.
26. Lawn, B., et al., *Failure modes in ceramic-based layer structures: A basis for materials design of dental crowns.* Journal of the American Ceramic Society, 2007. **90**(6): p. 1671-1683.
27. Currey, J.D. and J.D. Taylor, *Mechanical behavior of some molluscan hard tissues.* Journal of Zoology, 1974. **173**(JUL): p. 395-406.
28. Sarikaya, M. and I.A. Aksay, *Biomimetics : design and processing of materials (aip series in polymers and complex materials).* 1995, New York: American Institute of Physics.
29. Barthelat, F., et al., *On the mechanics of mother-of-pearl: A key feature in the material hierarchical structure.* Journal of the Mechanics and Physics of Solids, 2007. **55**(2): p. 306-337.
30. Meyers, M.A., et al., *Mechanical strength of abalone nacre: Role of the soft organic layer.* Journal of the Mechanical Behavior of Biomedical Materials, 2008. **1**(1): p. 76-85.
31. Wegst, U.G.K. and M.F. Ashby, *The mechanical efficiency of natural materials.* Philosophical Magazine, 2004. **84**(21): p. 2167-2186.
32. Li, X.D., et al., *Nanoscale structural and mechanical characterization of a natural nanocomposite material: The shell of red abalone.* Nano Letters, 2004. **4**(4): p. 613-617.
33. Graham, T. and M. Sarikaya, *Growth dynamics of red abalone shell: a biomimetic model.* Materials Science & Engineering C-Biomimetic and Supramolecular Systems, 2000. **11**(2): p. 145-153.
34. Zolotoyabko, E. and B. Pokroy, *Biomineralization of calcium carbonate: structural aspects.* Crystengcomm, 2007. **9**: p. 1156-1161.

35. Zaremba, C.M., et al., *Critical transitions in the biofabrication of abalone shells and flat pearls.* Chemistry of Materials, 1996. **8**(3): p. 679-690.
36. Sanchez, C., H. Arribart, and M.M.G. Guille, *Biomimetism and bioinspiration as tools for the design of innovative materials and systems.* Nature Materials, 2005. **4**(4): p. 277-288.
37. Wang, R.Z., et al., *Deformation mechanisms in nacre.* Journal of Materials Research, 2001. **16**(9): p. 2485-2493.
38. Wise, S.W., *Microarchitecture and mode of formation of nacre (Mother-of-Pearl) in pelecypods, gastropods, and cephalopods.* EcIogac Geologicae Helvetiae, 1970. **63**: p. 775-797.
39. Currey, J.D., *Mechanical properties of mother of pearl in tension.* Proceedings of the Royal Society of London Series B-Biological Sciences, 1977. **196**(1125): p. 443-463.
40. Lin, A. and M.A. Meyers, *Growth and structure in abalone shell.* Materials Science and Engineering a-Structural Materials Properties Microstructure and Processing, 2005. **390**(1-2): p. 27-41.
41. Lin, A.Y.M., P.Y. Chen, and M.A. Meyers, *The growth of nacre in the abalone shell.* Acta Biomaterialia, 2008. **4**(1): p. 131-138.
42. Schaffer, T.E., et al., *Does abalone nacre form by heteroepitaxial nucleation or by growth through mineral bridges?* Chemistry of Materials, 1997. **9**(8): p. 1731-1740.
43. Jackson, A.P., J.F.V. Vincent, and R.M. Turner, *The mechanical design of nacre.* Proceedings of the Royal Society of London Series B-Biological Sciences, 1988. **234**(1277): p. 415-440.
44. Sarikaya, M., *An introduction to biomimetics- a structural viewpoint.* Microscopy Research and Technique, 1994. **27**(5): p. 360-375.
45. Sarikaya, M. and I.A. Aksay, *Nacre of abalone shell: a natural multifunctional nanolaminated ceramic-polymer composite material*. Results and Problems in Cell Differentiation in Biopolymers. 1992, Amsterdam: Springer.
46. Sarikaya, M., et al., *Mechanical property-microstructural relationships in abalone shell.* Journal of Materials Research Society, 1990. **174**: p. 109-116.
47. Menig, R., et al., *Quasi-static and dynamic mechanical response of Haliotis rufescens (abalone) shells.* Acta Materialia, 2000. **48**(9): p. 2383-2398.
48. Barthelat, F. and H.D. Espinosa, *An experimental investigation of deformation and fracture of nacre-mother of pearl.* Experimental Mechanics, 2007. **47**(3): p. 311-324.
49. Gao, H.J., et al., *Materials become insensitive to flaws at nanoscale: Lessons from nature.* Proceedings of the National Academy of Sciences of the United States of America, 2003. **100**(10): p. 5597-5600.
50. Barthelat, F., et al., *Mechanical properties of nacre constituents and their impact on mechanical performance.* Journal of Materials Research, 2006. **21**(8): p. 1977-1986.

51. Evans, A.G., et al., *Model for the robust mechanical behavior of nacre.* Journal of Materials Research, 2001. **16**(9): p. 2475-2484.
52. Song, F. and Y.L. Bai, *Effects of nanostructures on the fracture strength of the interfaces in nacre.* Journal of Materials Research, 2003. **18**(8): p. 1741-1744.
53. Katti, D.R. and K.S. Katti, *Modeling microarchitecture and mechanical behavior of nacre using 3D finite element techniques - Part I - Elastic properties.* Journal of Materials Science, 2001. **36**(6): p. 1411-1417.
54. Katti, D.R., et al. *3D finite element modeling of mechanical response in nacre-based hybrid nanocomposites*. 2001: Elsevier Sci Ltd.
55. Ji, B.H. and H.J. Gao, *Mechanical properties of nanostructure of biological materials.* Journal of the Mechanics and Physics of Solids, 2004. **52**(9): p. 1963-1990.
56. Katti, K.S., et al., *Platelet interlocks are the key to toughness and strength in nacre.* Journal of Materials Research, 2005. **20**(5): p. 1097-1100.
57. Dashkovskiy, S., et al., *Nacre properties in the elastic range: Influence of matrix incompressibility.* Computational Materials Science, 2007. **41**(1): p. 96-106.
58. Tushtev, K., M. Murck, and G. Grathwohl, *On the nature of the stiffness of nacre.* Materials Science & Engineering C-Biomimetic and Supramolecular Systems, 2008. **28**(7): p. 1164-1172.
59. Kotha, S.P., Y. Li, and N. Guzelsu, *Micromechanical model of nacre tested in tension.* Journal of Materials Science, 2001. **36**(8): p. 2001-2007.
60. Bertoldi, K., D. Bigoni, and W.J. Drugan, *Nacre: An orthotropic and bimodular elastic material.* Composites Science and Technology, 2008. **68**(6): p. 1363-1375.
61. Almqvist, N., et al., *Methods for fabricating and characterizing a new generation of biomimetic materials.* Materials Science & Engineering C-Biomimetic and Supramolecular Systems, 1999. **7**(1): p. 37-43.
62. Clegg, W.J., et al., *A simple way to make tough ceramics.* Nature, 1990. **347**(6292): p. 455-457.
63. Dabbs, D.M. and I.A. Aksay, *Self-assembled ceramics produced by complex-fluid templation.* Annual Review of Physical Chemistry, 2000. **51**: p. 601-622.
64. He, J.L., et al., *Simulation of nacre with TiN/Pt multilayers and a study of their mechanical properties.* Materials Science and Engineering B-Solid State Materials for Advanced Technology, 1997. **49**(2): p. 128-134.
65. Tang, Z.Y., et al., *Nanostructured artificial nacre.* Nature Materials, 2003. **2**(6): p. 413-418.
66. Caspi, E.N., et al., *On the structure of aragonite.* Acta Crystallographica Section B: Structural Science, 2005. **61**(2): p. 129-132.
67. Kanit, T., et al., *Determination of the size of the representative volume element for random composites: statistical and numerical approach.* International Journal of Solids and Structures, 2003. **40**(13-14): p. 3647-3679.

68. Fitoussi, J., G. Guo, and D. Baptiste, *Determination of a tridimensional failure criterion at the fibre/matrix interface of an organic-matrix/discontinuous-reinforcement composite.* Composites Science and Technology, 1996. **56**(7): p. 755-760.
69. Stamblewski, C., B.V. Sankar, and D. Zenkert, *Analysis of three-dimensional quadratic failure criteria for thick composites using the direct micromechanics method.* Journal of Composite Materials, 2008. **42**(7): p. 635-654.
70. Wang, C.H., L.C. Zhang, and Y.W. Mai, *Deformation and fracture of macadamia nuts .1. deformation analysis of nut-in-shell.* International Journal of Fracture, 1994. **69**(1): p. 51-65.
71. Fischer-Cripps, A.C., *Introduction to contact mechanics*. Second ed. 2007, New York: Springer.
72. Courtney, T.H., *Mechanical behavior of materials*. 1990: McGraw-Hill New York.
73. Arora, J.S., *Introduction to optimum design*. 2004, Amsterdam; Boston: Elsevier/Academic Press.
74. Deb, K. and D. Kalyanmoy, *Multi-Objective Optimization Using Evolutionary Algorithms*. 2001, New York: John Wiley & Sons, Inc. 518.
75. Ghiasi, H., D. Pasini, and L. Lessard, *Optimum stacking sequence design of composite materials Part I: Constant stiffness design.* Composite Structures, 2009. **90**(1): p. 1-11.
76. Du, D. and P.M. Pardalos, *Handbook of combinatorial optimization*. 1998, Boston: Kluwer Academic Publishers.
77. Spall, J.C., *Introduction to stochastic search and optimization*. 2003, New York; Chichester: Wiley.
78. Holland, J.H., *Adaptation in natural and artificial systems*. 1975, Ann Arbor: University of Michigan Press.
79. Kirkpatrick, S., C.D. Gelatt, and M.P. Vecchi, *Optimization by simulated annealing.* Science, 1983. **220**(4598): p. 671-680.
80. Horst, R., P.M. Pardalos, and N.V. Thoai, *Introduction to global optimization*. Nonconvex optimization and its applications, v. 3. 1995, Dordrecht; Boston: Kluwer Academic Publishers.
81. Nelder, J.A. and R. Mead, *A simplex-method for function minimization.* Computer Journal, 1965. **7**(4): p. 308-313.
82. Barton, R.R. and J.S. Ivey, *Nelder-Mead simplex modifications for simulation optimization.* Management Science, 1996. **42**(7): p. 954-973.
83. Lagarias, J.C., et al., *Convergence properties of the Nelder-Mead simplex method in low dimensions.* Siam Journal on Optimization, 1998. **9**(1): p. 112-147.
84. Han, L.X. and M. Neumann, *Effect of dimensionality on the Nelder-Mead simplex method.* Optimization Methods & Software, 2006. **21**(1): p. 1-16.
85. Luersen, M.A. and R. Le Riche. *Globalized Nelder-Mead method for engineering optimization*. 2004.

86. Huzak, M. and Z. Bajzer. *A new algorithm for global minimization based on the combination of adaptive random search and simplex algorithm of Nelder and Mead*. 1996.
87. Offord, C. and Z. Bajzer, *A Hybrid Global Optimization Algorithm Involving Simplex and Inductive Search*, in *Proceedings of the International Conference on Computational Science-Part II*. 2001, Springer-Verlag.
88. McKinnon, K.I.M., *Convergence of the Nelder-Mead simplex method to a nonstationary point.* Siam Journal on Optimization, 1998. **9**(1): p. 148-158.
89. Weaver, P.M. and M.F. Ashby, *Material limits for shape efficiency.* Progress in Materials Science, 1997. **41**(1-2): p. 61-128.